System-Level Design Analysis for Large Rotors – Pre-print, to be submitted to Wind Energy Science

Daniel S. Zalkind[1], Gavin K. Ananda[2], Mayank Chetan[3], Dana P. Martin[4], Christopher J. Bay[1,4], Kathryn E. Johnson[4], Eric Loth[5], D. Todd. Griffith[3], Michael S. Selig[2], and Lucy Y. Pao[1]

[1]Boulder, CO 80309
[2]Champaign, IL
[3]800 W Campbell Rd, Richardson, TX 75080
[4]1500 Illinois St, Golden, CO 80401
[5]Charlottesville, VA

Correspondence: Daniel S. Zalkind (dan.zalkind@gmail.com)

Abstract. We examine the impact of different rotor design choices on the power capture and structural loading of each major wind turbine component. A steady-state, harmonic model using aeroelastic simulations in the NREL FAST code is developed to reduce computational expense while evaluating design trade-offs for the structural loading on rotors with diameters greater than approximately 100 m. We provide an overview of wind turbine loads, as well as their relationship to one another and the turbine design parameters that influence them. A number of detailed design studies are performed, which focus on blade aerodynamic and structural parameters as well as different hub configurations and nacelle placements. The effects of tower design and closed-loop control are also analyzed. Design loads are calculated according to the IEC design standards and used to calibrate the harmonic model and quantify uncertainty.

Our design studies highlight both industry trends and innovative designs: we progress from a conventional, upwind, 3-bladed rotor, to a rotor with longer, more slender blades that is downwind and 2-bladed. We show that increasing the blade length by 25 m while decreasing the induction factor of the rotor increases annual energy capture by 11% while constraining peak blade loads. A downwind, 2-bladed rotor design is analyzed, with a focus on its ability to reduce peak blade loads by 10% per 5 deg. of coning, and also reducing total blade mass. However, when compared to conventional, 3-bladed upwind designs, the peak main bearing load of the up-scaled, downwind, 2-bladed rotor is increased by 280%. Optimized teeter configurations and individual pitch control can reduce non-rotating damage equivalent loads by 45% and 22%, respectively, compared with fixed-hub designs.

1 Introduction

Wind turbines are large, dynamic structures that experience significant structural loading on their component parts. Design choices impact the loading on each of these parts. We present a model for the rapid computation of wind turbine design loads, which we use to quantify the effect of design trade-offs associated with different rotor concepts. Economies of scale have enabled larger wind turbine sizes, generator ratings, and blade lengths. Longer blades are economical simply because they

capture more power more often. A wind turbine's annual energy production (AEP) is the total amount of energy captured by a wind turbine during one year. Increasing the power capture is the primary driver of reducing the cost of wind energy (COE)

$$\text{COE} = \frac{\text{CapEx} + \text{OpEx}}{\text{AEP}}, \tag{1}$$

where capital expenditures (CapEx) and operational expenditures (OpEx) make up the cost of building and running a wind turbine. Our goal is to minimize the cost of wind energy, enabling the sale of more wind turbines in an effort to meet our climate goals.

Operational expenditures are non-negligible, but make up roughly 15% of the total cost, according to a study of the average 2015 offshore wind turbine (Mone et al., 2015). Capital expenditures are comprised of a large component, making up about 55% of the total cost, called the balance-of-station cost, which includes electrical infrastructure, assembly, and substructure costs. A comparably smaller portion (about 30%) in Mone et al. (2015) of the overall cost of wind energy is for the wind turbine components themselves, and only a fraction of that portion is attributed to the blades. The small cost contribution of the wind turbine blades and their significant effect on AEP contribute to the economics that enable larger and larger blades.

However, longer blades require additional structural reinforcement, which increases the blade weight, resulting in larger loads experienced by other wind turbine components: like the hub, main bearing, yaw bearing, and tower. Various innovations have enabled lower weight blades; these innovations are then used to subsequently design larger blades that capture more power. Still, the wind turbine components must survive extreme structural loading and last 20-30 years. Wind turbine components are often designed by various engineering teams, initially based on loads from aeroelastic simulations, making wind turbine design a very large, distributed design task.

The aerodynamic and structural aspects of wind turbines must be designed and controlled so that the structural loading for a design is feasible. There is a large inter-dependence between these design aspects (aerodynamic, structural, and controls) and on the various wind turbine components, which has led to numerous design optimization studies. These studies focus primarily on blade aerodynamic and structural design, e.g., in Ning et al. (2014) and Pavese et al. (2017). Some incorporate dynamic control effects, like in Tibaldi et al. (2015) and Bortolotti et al. (2016). System engineering tools like HAWTOpt2 (Døssing, 2011), WISDEM (Dykes et al., 2015), and Bottasso et al. (2012), have been developed to handle the large number of necessary design variables, but often compute structural loads using simplified scaling rules or hundreds of nonlinear aeroelastic simulations. These load calculations can be costly in terms of computational effort and in design cycle time. A full suite of design load cases (DLCs), specified by the International Electrotechnical Commission (2005) (IEC) in design standards, and simplified for research purposes in Natarajan et al. (2016), can include up to 2000 simulations. Often the results of these simulations do not fully elucidate the root cause of problematic load cases on the affected turbine component. An attempt to distill the DLCs into a reduced basis for design loads in an optimization framework was presented in Pavese et al. (2016).

We will provide an alternative, based on a set of quasi-steady simulations that illustrates the main drivers of wind turbine loads and the effects of design changes on global wind turbine loads. Since both turbulent and steady wind effects contribute to structural loading and the effect of turbulence has been well studied recently, e.g., in Dimitrov et al. (2017) and Robertson et al. (2018), we will focus our effort on how turbine model changes impact the steady loads caused by wind shear and turbine

self-weight. We will do this by decomposing the turbine loads into their harmonic components, i.e., the load amplitude of the n-per-revolution (nP) load signal. These signals have been used for control (Bottasso et al., 2013), stability analysis (Bottasso and Cacciola, 2015), and wind field estimation (Bertelè et al., 2017). Here, we will use the same signals for model development in order to understand the effect that changing the underlying turbine model has on steady and azimuthally-dependent wind turbine loads.

In this study we will analyze large rotor concepts. A number of reference designs have been published along with design studies from the European projects UpWind and INNWIND. The Danish Technical University (DTU) 10 MW Reference Wind Turbine (RWT) (Bak et al., 2013), was provided as a design basis for large rotors to test design methods and tools. The DTU 10 MW RWT has motivated studies that focus on optimization methods (Zahle et al., 2015), active (McWilliam et al., 2018), and passive (Pavese et al., 2017) load control methods, operating within the confines of the base rotor model. A two-bladed, downwind, teetering hub configuration of the DTU 10 MW RWT was developed, which shows that a teetering hub can greatly reduce the unbalanced loading on the main shaft and blade root (Bergami et al., 2014). However, the authors suggest that the tower stiffness distribution needs to be redesigned in order to avoid a resonance at the twice-per-revolution (2P) rotor harmonic and that 2-bladed rotors (without teeter) increase loading on the main shaft significantly.

A couple of 20 MW rotor designs have been proposed in the literature. Sieros et al. (2012) and Peeringa et al. (2011) use classical similarity scaling rules to upscale conventional turbines. Both conclude that loads due to self-weight will increase significantly with blade length and drive component design as turbines grow larger. Specifically, edgewise blade loads and the effect of wind shear are magnified for larger rotor sizes.

A series of design studies at Sandia National Laboratories (SNL) detailed the structural design of a 100 m blade, with the goal of reducing the blade mass. First, a classically upscaled blade was given a detailed composite layup and geometry, and tested against design load cases (Griffith and Ashwill, 2011). Next, a series of design innovations reduced the blade mass from 76 metric tons to 49 metric tons, utilizing carbon fiber reinforcement (Griffith, 2013a), advanced core materials (Griffith, 2013b), and flatback airfoils (Griffith and Richards, 2014).

Another concept to reduce mass-scaling issues is a highly coned, downwind rotor, which has shown that blade loads can be reduced by converting large cantilever loads at the blade root into tensile loads along the span of the blade (Ichter et al., 2016; Loth et al., 2017). We will analyze this concept and its effect on the structural loading of the other wind turbine components besides the blades.

There are few openly published documents that quantify the effects of significant design changes and detailed rotor upscaling on the various wind turbine components. We will quantify the effect of aerodynamic changes, including the blade length, axial induction, cone angle, and number of blades, as applied to both upwind and downwind rotors. A simplified structural model will demonstrate the effect of structural reinforcement on blade properties and loads. The upscaled structural model must provide enough stiffness to compensate for the increasing edgewise blade loads of large rotors. We quantify the effect of changes to the hub by looking at 3-bladed and 2-bladed rotor configurations, and consider the effects of a potentially necessary teeter hinge or individual pitch control for the latter. Finally, we show how the layout of the nacelle and control schemes can impact the loads on the tower and yaw bearing.

We believe this study will contribute an early-stage design model for evaluating design concepts more quickly in simulation by eliminating 100s of DLC simulations. We also present a qualitative understanding of the relationship between wind turbine structural loads as they progress from the blades to the substructure, highlighting the areas where peak and fatigue loads are most problematic. A quantitative design study will evaluate the effect of increased blade size and power capture on global wind turbine loads, as well as the design trade-offs associated with 2-bladed wind turbines, teeter hinges, and individual pitch control. Finally, we calibrate the model against a full set of design load cases and quantify the uncertainty.

We will present the baseline models used for comparison and our general design direction in Section 2. Section 3 will outline the tools used for design and simulation, and it will also provide environmental site specifics. A steady-state harmonic model is described in Section 4 and Section 5 provides a qualitative understanding of the wind turbine loads. Design studies are described and presented in Section 6. The model is calibrated and its uncertainty is quantified in Section 7, followed by some conclusions in Section 8.

2 Baseline Models and Design Direction

It is useful to start from established designs when doing comparative analysis. In Section 6.2, in lieu of a full structural layup design, we will use these baseline models for scaling the distributed structural properties of rotor blades. For 3-bladed rotors, we will use the a conventional design (CONR-13) as a starting point. The CONR-13 is the culmination of a series of design studies aimed at designing the lightest 100 m blade; it utilizes flatback airfoils, carbon fiber reinforcement, and advanced core materials to reduce the blade mass below state-of-the-art scaling trends. The full design is described in Griffith and Richards (2014). The distributed properties of the CONR-13 will be used for all 3-bladed rotors in this study.

A downwind, 2-bladed rotor was developed with similar structural advances, but with the goal of reducing the total blade mass by at least 25% compared to the CONR-13 (Paquette, 2017). The blade was designed to enable segmentation, ultralight design, and a morphing rotor (SUMR-13A). The initial aerodynamic design is presented in Ananda et al. (2018). We have slightly modified the initial design to have a cone angle of 5 deg. for the purposes of the design studies presented later. The distributed structural parameters of the SUMR-13A blade were used as a basis for scaling all 2-bladed rotors in this study. A summary of both baseline models is shown in Table 1. Both rotors were structurally validated to check strain limits, panel buckling, flutter, and fatigue.

In the remainder of this paper, we will evaluate designs aimed at

1. increasing the energy capture, and

2. reducing the wind turbine component loads.

To reduce the cost of energy (1), it is most important to increase energy capture (AEP). Industry trends suggest larger and larger blades, which lead to increased blade mass and greater loads on all turbine components. Structural loads contribute to component design and capital cost (CapEx), but require detailed design and cost models for each individual part. Instead of a detailed cost analysis, which is specific to the component supplier and subject to uncertainty, we will develop a larger rotor

Table 1. Baseline turbine models and new design presented in this study as well as environmental parameters used for design.

Turbine Model	**CONR-13**	**SUMR-13A**	**SUMR-13B**
Rated Power	13.2 MW	13.2 MW	13.2 MW
Rated Rotor Speed	7.44 rpm	9.90 rpm	7.99 rpm
Hub Height	142.4 m	142.4 m	142.4 m
Rotor Radius	102.5 m	101.2 m	125.4 m
Rotor Position	Upwind	Downwind	Downwind
Blade Mass	49.5 Mg	51.8 Mg	64.7 - 89.2 Mg
Number of Blades	3	2	2
Max Chord	5.23 m	7.22 m	6.79 m
Cone Angle	-2.5 deg.	5 deg.	12.5 deg.

Environmental Parameters	
Wind Turbine Site Class	Class IIB
Mean wind speed at 50 m, hub height	7.87, 9.11 m/s
Weibull shape, scale factor	2.17, 10.3
Turbulence Intensity at 15 m/s	0.14

design, called the SUMR-13B, described in Section 6.1, and then quantify the changes to global wind turbine loads, while exploring techniques to reduce those loads.

3 Design and Simulation Tools, Wind Turbine Environment

Aerodynamic design was performed using two inverse design tools: PROPID and PROFOIL. PROPID (Selig and Tangler, 1995; Selig, 1995-) is an inverse rotor design tool that enables a rotor geometry to be designed based on desired performance specifications such as power, tip speed ratio, wind speed distribution, axial induction, airfoils used, and desired lift distribution along the blade. PROFOIL (Drela, 1987, 1989) is an inverse airfoil design tool. It allows for the design of airfoil geometries based on prescribed velocity distributions and desired geometric (thickness and camber) and aerodynamic properties (moment). Airfoil geometries output using PROFOIL are analyzed using XFOIL and iterated on using PROFOIL until a final converged design is obtained.

PROPID determines the rotor geometry when given desired performance specifications from the designer, including power, tip speed ratio, a wind speed distribution, and axial induction along the blade span. PROFOIL is similar, but used for airfoil design. Structural design was performed using NuMAD (Berg and Resor, 2012). The structural layup design in NuMAD allows for detailed material stacking and placement along the blade.

Aeroelastic simulations were performed using the latest version of FAST (Jonkman, 2013). Different FAST modules couple wind inflow with aerodynamic and elastic solvers that compute the structural loading on the wind turbine. Turbulent wind inputs are generated using TurbSim (Jonkman and Kilcher, 2012). Recent studies have shown that, compared with turbulence, tower shadow effects are relatively small (Noyes et al., 2018) and that tower fairings have been shown to greatly reduce the tower wake (Larwood and Chow, 2016). Thus, for simplicity, we have omitted a tower shadow model from our analysis. Control inputs (generator torque and pitch) are provided to FAST through a Matlab/Simulink interface that processes FAST outputs and performs closed-loop control. Fatigue results are computed using MLife (Hayman, 2012), which uses a rainflow counting algorithm to determine load cycles and extrapolates them over the lifetime of the wind turbine.

To properly compute lifetime fatigue and annual energy production, the wind turbine environment must be provided. The rotors in this study are all designed to be placed off the coast of Virginia, USA. The site corresponds to a Class IIB turbine rating, with mean and turbulent wind speed characteristics shown in Table 1.

4 Harmonic Model for Load Estimation

Load simulations according to the Design Load Cases (DLCs) can be time consuming, so we have developed a simplified model to estimate the loads on wind turbine components more quickly for evaluating design trade-offs. The model runs FAST simulations with a sheared wind inflow such that the wind speed u at height z is

$$u(z) = u_h \left(\frac{z}{z_h} \right)^{\alpha}, \tag{2}$$

where z_h is the hub height, u_h is the wind speed at hub height, and $\alpha = 0.14$, which is representative of an offshore wind field. The simulations reach a steady state after some time. Because of the wind shear, the load signals contain harmonic components that depend on the rotor azimuth ψ, i.e., a load signal $m(\psi)$ can be expressed as

$$m(\psi) = m_0 + m_c^{1\mathrm{P}} \cos(\psi) + m_s^{1\mathrm{P}} \sin(\psi) + ... + m_c^{i\mathrm{P}} \cos(i\psi) + m_s^{i\mathrm{P}} \sin(i\psi) + ... \tag{3}$$

The components are computed by

$$m_0 = \frac{1}{2\pi N_R} \int_{\psi - 2\pi N_R}^{\psi} m(\psi) d\psi, \tag{4}$$

$$m_c^{i\mathrm{P}} = \frac{1}{2\pi N_R} \int_{\psi - 2\pi N_R}^{\psi} m(\psi) \cos(i\psi) d\psi, \tag{5}$$

and

$$m_s^{i\mathrm{P}} = \frac{1}{2\pi N_R} \int_{\psi - 2\pi N_R}^{\psi} m(\psi) \sin(i\psi) d\psi, \tag{6}$$

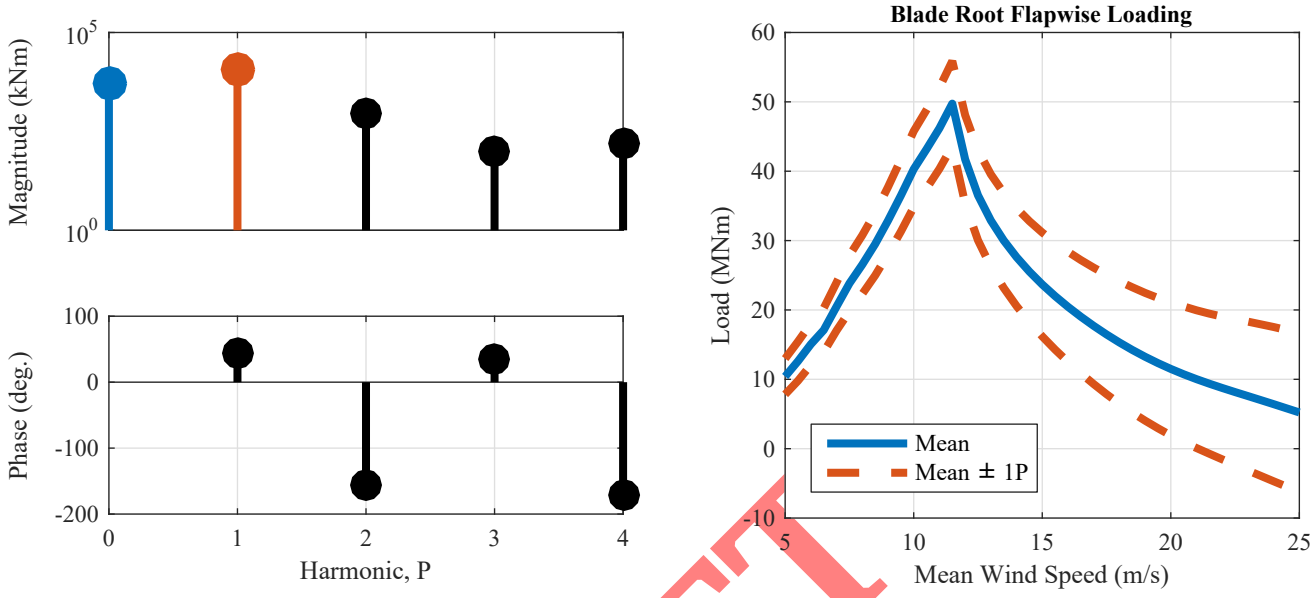

Figure 1. Load harmonic magnitude $|m^{i\mathrm{P}}|$ and phase $\phi^{i\mathrm{P}}$ for the 0th through 4th periodic harmonic of the blade root load in the flapwise direction (left). Mean load (right, blue) superimposed with the 1P harmonic amplitude with respect to wind speed (right, red) used to estimate fatigue and extreme loads.

where N_R is the number of rotations used in the calculation. The load signals can be reconstructed closely using the first four harmonics; the most energy is usually in either the 1st, 2nd, or 3rd harmonic depending on the component (see Table 2).

From the components in (5) and (6), the magnitude and phase of each harmonic can be computed,

$$|m^{i\mathrm{P}}| = \sqrt{(m_c^{i\mathrm{P}})^2 + (m_s^{i\mathrm{P}})^2}, \tag{7}$$

and

$$\phi^{i\mathrm{P}} = \tan^{-1}\left(\frac{m_s^{i\mathrm{P}}}{m_c^{i\mathrm{P}}}\right). \tag{8}$$

An example for the blade flapwise load is shown in Fig. 1. We will use these harmonic coefficients to estimate fatigue and extreme loads for the various wind turbine components.

5 Component Loads

Structural loads originate from the interaction of the wind with the blades, transferring through the blade root (b) to the hub (h) at the pitch actuator. The rotating hub is connected to the main shaft, which is supported by a main bearing (m). The loads transfer from the main bearing to the yaw bearing (y) via the nacelle bedplate and finally into the tower, which connects to the substructure at the tower base (t). The load locations are shown in Fig. 2.

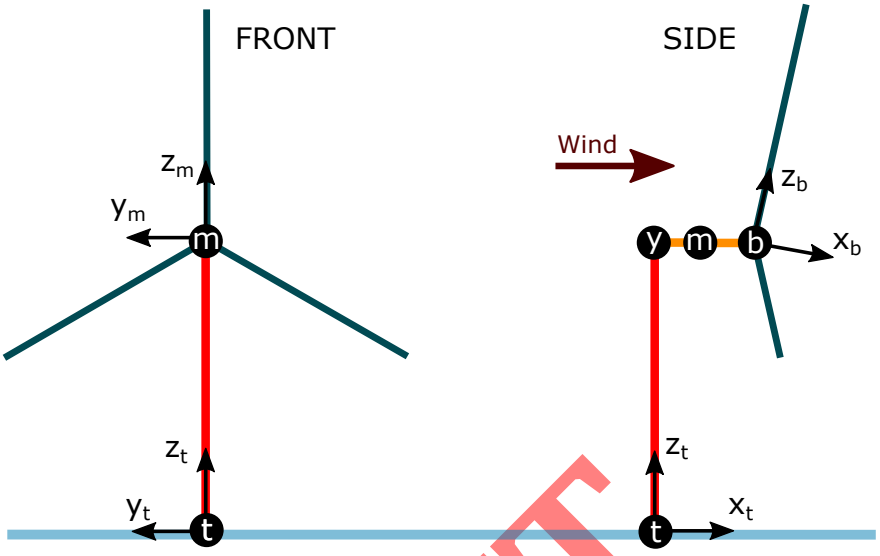

Figure 2. Illustration of the load axes used in this article. The non-rotating loads (tower, main bearing, and yaw bearing) are all parallel, denoted by a subscript t, m, and y, respectively. Blade and hub load axes rotate with azimuth angle, as shown in Fig. 3. A downwind rotor is depicted; the wind is in the same direction as the x_t axis.

5.1 Extreme and Fatigue Loads

The forces and moments on a component drive its design: larger loads require greater reinforcement, leading to greater component mass and cost. We analyze component loads in terms of the maximum (or peak) load

$$m^{\text{peak}} = \max_{u \in U}(m^0 + m^n), \tag{9}$$

where U is the set of steady-state wind speed simulations in the study. We do simulations from cut-in to cut-out (Table 1) in 0.5 m/s increments. Fatigue weakens materials through repeated load cycles. The damage equivalent load (DEL) is the constant amplitude of a sinusoidal load signal that results in the same total accumulated damage from a more complex load signal. The accumulated damage in simulations with different wind speeds is extrapolated over the turbine lifetime using the wind speed probability distribution $p(u)$, specified in Table 1. We can relate the DEL of a component to its load harmonic by

$$m^{\text{DEL}} = a_{\text{DEL}}(n, w) \sum_{u \in U} p(u) m^{n\text{P}} \tag{10}$$

where n specifies the dominant harmonic signal component and a_{DEL} is a tuning factor that depends on the Whöler exponent w and n. The dominant load harmonic of each component is either 1P or N_BP, specified in Table 2, depending on whether the component is rotating (1P) or non-rotating (N_BP). Blade and hub loads are computed in the rotating frame about the axes (load directions) specified in Table 2 and shown in Figs. 2 and 3. Different load harmonics will be specified by their location, direction, and harmonic number, e.g., the 3P main bearing load in the y-direction will be written $m^{3\text{P}}_{my}$. The load components and directions studied in this paper are specified in Table 2.

Table 2. Structural loads evaluated in the current design studies. Each component has loads in multiple directions and experiences the peak load and greatest contribution to fatigue loads at different wind speeds. N_B denotes the number of blades on the rotor.

Component	Dominant Harmonic	Load Direction, Name	Peak Wind Speed	Fatigue Wind Speed
Blade	1P	Flapwise, m_{by}	rated	rated
		Edgewise, m_{bx}	near constant	below rated
Shaft	1P	Tilt m_{hy}	near constant	rated
		Yaw, m_{hz}	near constant	rated
Main Bearing	N_BP	Tilt m_{my}	rated/cut-out	rated
		Yaw, m_{mz}	rated/cut-out	rated
Yaw Bearing	N_BP	Tilt, m_{yy}	rated/cut-out	rated
		Yaw, m_{yz}	rated/cut-out	rated
Tower	N_BP	Fore-aft, m_{ty}	rated	tower natural freq.
		Side-to-side, m_{tx}	tower natural freq./cut-out	tower natural freq.

5.2 Blade Loads

Blade loads are computed at the blade root in the flapwise (m_{by}) and edgewise (m_{bx}) directions. Blade flapwise loads are primarily aerodynamic in nature, depending on the thrust force exerted on the blades from the wind inflow. Extreme blade flapwise loads occur near rated wind speed, at the maximum wind speed before the blade begins pitching to regulate power in above-rated operation. Since the blade pitch has such an influence on the DC component of the blade flapwise load, control actions can often cause peak loads, e.g., when the pitch angle decreases to optimize power and then a wind speed gust occurs. The dependence of this load on the control system highlights the necessity of including control design at an early stage.

Flapwise fatigue loads are highly dependent on turbulence, driven by blade thrust and wind shear. Edgewise loads on the other hand, have a near zero mean, so we only focus on the fatigue loading, which depends primarily on the blade weight since the blade experiences a fully reversing load cycle during each rotation. Edgewise fatigue loads increase exponentially with blade length, and are a driving design case for the baseline blade structures used in this study. Additional stiffness can compensate for these increased loads, but further increase mass. We will explore this relationship in Section 6.2.1.

5.3 Hub Loads

Hub loads are also near zero-mean, so we only focus on their fatigue loading. Loads on the hub are transferred from the blade root through the pitch bearing; their axes rotate with the hub (Fig. 3). In the y-direction, hub loads are directly related to the blade loads for both 2- and 3-bladed configurations and peak when the rotor is near $\psi = 0$, meaning that the cosine-cyclic component of the hub load in the y-direction ($m^{1P}_{hy,c}$) is large. A teeter hinge reduces the coupling between blade and hub loads. In the z-direction, the source of loading is dependent on whether the rotor has 2 or 3 blades (see Fig. 3). For 3-bladed

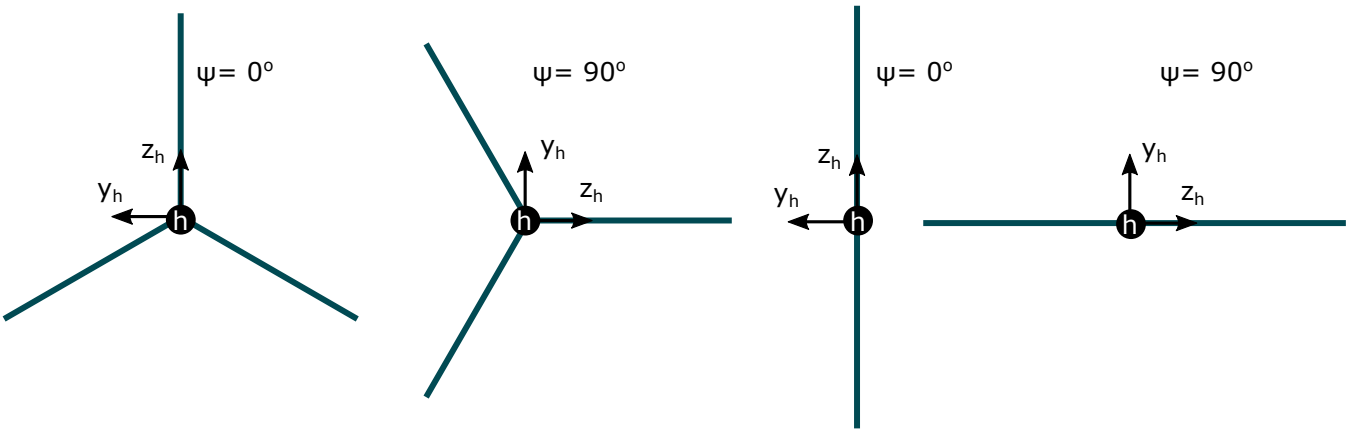

Figure 3. The hub axis (h) as it rotates with the the rotor azimuth angle ψ for a 3- and 2-bladed rotor.

rotors, the hub load is still driven by the blade load and the 1P magnitude is the same as in the y-direction. This symmetry is not inherent in a 2-bladed configuration; the m_{hz} load is primarily determined by the weight of the blades unless there is a horizontal wind shear. The hub load in the z-direction, for both hub configurations, peaks when the rotor is at $\psi = 90°$, resulting in a large $m^{1P}_{hz,s}$ component. The magnitude of these loads in relation to each other is important for determining their impact on the non-rotating load components, as we will investigate in Section 6.3.

5.4 Main Bearing and Yaw Bearing Loads

Hub loads are transferred to the rest of the turbine through the main bearing, which supports the low-speed-shaft close to the hub and also may consist of additional bearings between the hub and gearbox. A rotation matrix can model the transfer of loads from the rotating to non-rotating frame

$$\begin{bmatrix} m_{my} \\ m_{mz} \end{bmatrix} = \begin{bmatrix} \cos\psi & -\sin\psi \\ \sin\psi & \cos\psi \end{bmatrix} \begin{bmatrix} m_{hy} \\ m_{hz} \end{bmatrix}, \tag{11}$$

which results in the 1P hub loads mapping to a large 0P and 2P load component. The main bearing must support the weight of the rotor and thrust imbalance on the rotor due to shear, i.e.

$$m^0_{my} = m^0_{my,\text{grav}} + m^0_{my,\text{shr}}. \tag{12}$$

For downwind turbines, both components of (12) are positive, resulting in large, constant main bearing loads in the y-direction. For upwind turbines, the the load due to gravity $m^0_{my,\text{grav}}$ is negative while the load due to wind shear $m^0_{my,\text{shr}}$ is positive, which greatly reduces the steady-state main bearing load for upwind turbines compared to downwind turbines. To quantify this effect, we focus on the effect of downwind cone angles on the peak tilt moment m^{peak}_{my}. We will quantify this effect in Section 6.3 and explore the relative impact with added turbulence in Section 7. The hub configuration, including the number of blades, whether

a teeter hinge is used, and individual pitch control all have an impact on the fatigue loading of the main bearing, which we will analyze in both the tilt and yaw directions.

The loading on the main bearing is computed in the non-rotating frame at the hub location. Using the distance from the hub to the main bearing, the forces at the location of the main bearing can be computed. The peak and fatigue moments on the main bearing occur near rated wind speeds and also near cut-out wind speed due to the high thrust and thrust imbalance due to shear on the rotor, respectively.

The main bearing is mounted to the bedplate of the nacelle, which attaches to the yaw bearing, responsible for rotating the entire nacelle and rotor to align with the wind direction. The yaw bearing experiences similar loads to the main bearing; they peak near rated and again at cut-out due to thrust effects. A potential issue with downwind turbines is the overturning moment on the yaw bearing, similar to the peak main bearing load. In this study, we have adjusted the nacelle center of mass to minimize the yaw bearing loads in 0 m/s.

5.5 Tower Loads

The tower must support the entire rotor-nacelle assembly and withstand a moment due to rotor thrust, resulting in very large loads, which we compute at the tower base. We present the peak fore-aft loading and the fatigue loading in the side-to-side direction. The fore-aft load depends primarily on the rotor thrust, with a peak near rated speed. Since there is no aerodynamic damping in the side-to-side direction, wind turbines can exhibit instabilities in this direction (Jonkman and Matha, 2011). Large, modern wind turbine towers are usually designed to be "soft-stiff", with a natural frequency between the 1P and 3P harmonic of the rotor (van der Tempel and Molenaar, 2003). If the same tower is used for a 2-bladed wind turbine, the 2P harmonic of the rotor and the natural frequency of the tower are more likely to overlap. One idea is to use a high-compliance tower structure (Bergami et al., 2014) or use a floating substructure, which has a natural frequency below the 1P harmonic. The issue with designing a tower with a very low natural frequency is the interaction of the tower and rotor motion with the speed regulation of the rotor. In this case, the speed regulator will perceive tower motion as a wind speed disturbance, and overcompensate. Several studies have considered this, given the emergence of floating wind turibines (Jonkman and Matha, 2011), but to simplify our analysis, we have kept the same tower for all turbines: a scaled version of the NREL-5MW reference model (Jonkman et al., 2009). To account for the instabilities that occur when the 2P harmonic overlaps with the tower natural frequency, we have designed a speed avoidance controller that avoids the rotor speed associated with this instability. We will quantify tower load differences in Section 6.5. Load increases in the tower need to be reinforced similarly to the other components, which is important because the tower makes up a large portion of the turbine cost: 20% of the average offshore wind turbine (Mone et al., 2015).

5.6 Steady vs. Turbulent Loads

The structural loads on a wind turbine originate from both steady-state effects, qualitatively described above, as well as from dynamics due to turbulence and wind direction changes. In some cases, the effect of turbulence greatly outweighs the steady effects, but in all cases, the steady-state effects predict, to some extent, changes in the design load determined by the DLCs.

We have quantified this relationship in Section 7 by calibrating the steady-state load estimates to the design loads. In the next section, we use the steady-state loads to present calibrated load estimates (and their uncertainty) as various design choices are evaluated.

6 Design Studies

In this section, we have designed and simulated 45 different turbine models and computed the harmonic load components using the method in Section 4. The loads were calibrated to DLC simulations to estimate design loads using a procedure that will be discussed in Section 7. Here, we present the calibrated load estimates along with their corresponding uncertainties. Power capture (AEP) was calculated using the generator power $P(u)$ at steady-state wind speed u by

$$AEP = \sum_{u \in U} p(u)P(u), \tag{13}$$

where $p(u)$ is the Weibull distribution in Table 1.

We will examine changes to the blade loads due to aerodynamic and structural design changes, leading to a longer, heavier SUMR-13B. Non-rotating component loads will be compared for different hub configurations, considering the number of blades, a teetering hinge, individual pitch control, and rotor placement (upwind vs. downwind). The effect of a downwind rotor on yaw bearing loads will be presented and the effect of a two-bladed rotor on tower design will be shown in addition to closed-loop control effects. A summary of the design parameters studied here is presented in Fig. 4.

6.1 Aerodynamics

We evaluate rotors with longer blade lengths, lower axial induction factors, and large, downwind cone angles, starting from the SUMR-13A design described in Section 2. These design studies have led us to an updated 2-bladed design, indicative of the trends in industry towards longer, more slender blades, but with a greater downwind cone angle. We will call this new rotor SUMR-13B (see Table 1 for more details).

The blade length is changed indirectly in PROPID, by increasing the available rotor power at 11.3 m/s from 13.9 MW to 16.9 MW. However, all rotors are controlled to have the same rated generator power of 13.2 MW, which constrains the peak blade loads by transitioning to above-rated control at lower wind speeds. For the blade length design study (blue, left in Fig. 5) the axial induction factor along the blade was fixed at ⅓ (theoretical Betz limit). The increased rotor swept area increases both power capture and blade loads; a 10 m increase in rotor radius results in about a 10% increase in AEP and 15% increase in peak load.

The axial induction design studies (red, center in Fig. 5) were conducted by fixing the flapwise root bending loads to that of the SUMR-13A. The power at rated speed was also fixed to 13.9 MW. The blade length, chord, and twist were allow to vary based on variation of the axial induction factor. Axial inductions factors were varied in increments of 0.025 from 0.175 to 0.3. These axial induction factors were fixed along the blade from the 25% radial location to the blade tip. Decreasing the designed axial induction of the rotor results in longer, more slender blades that capture more energy and constrain blade

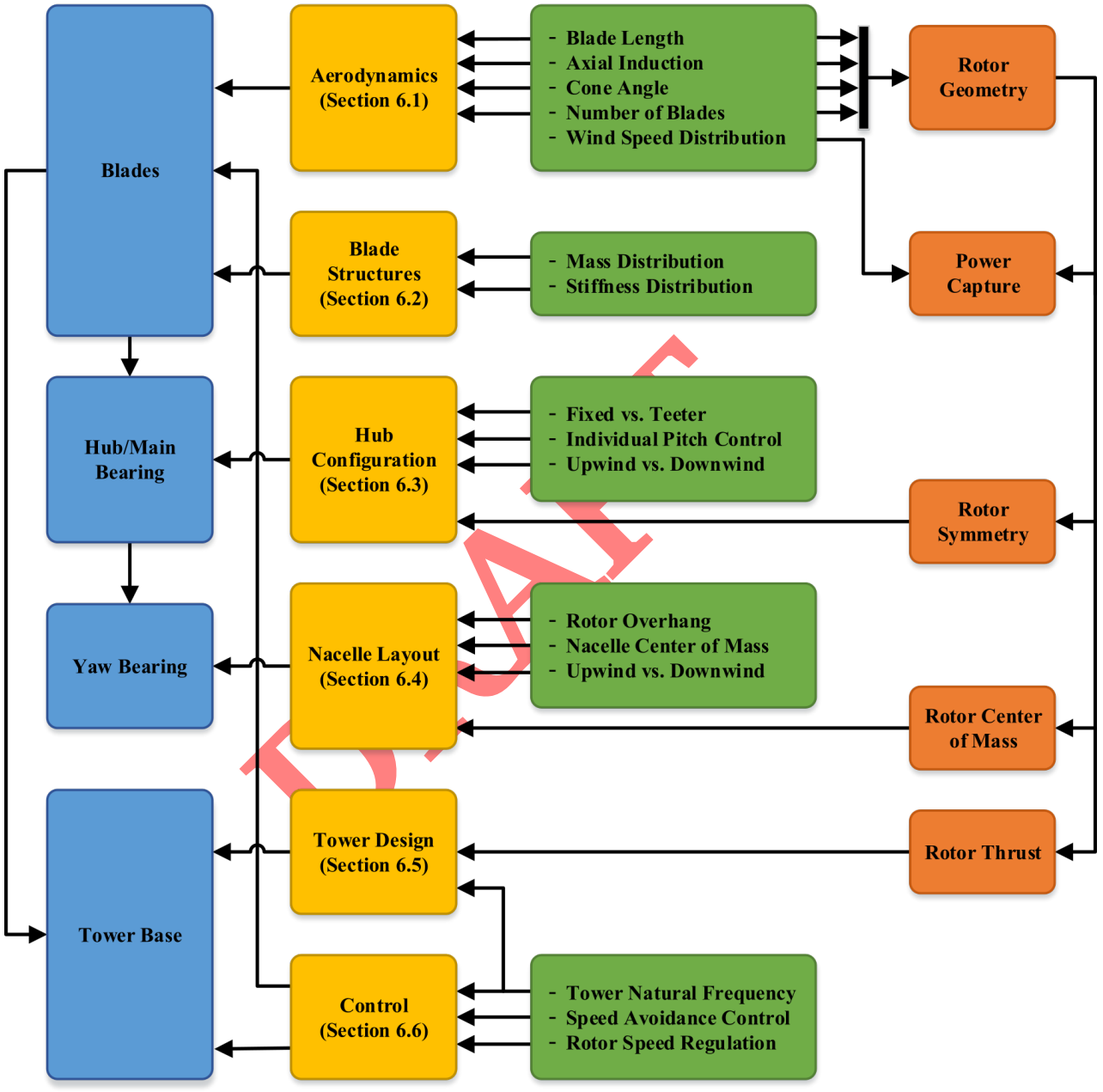

Figure 4. Overview of the design studies performed in this paper. The loads on each component (left) transfer from the wind to the blades to the tower base. Design studies (yellow) that affect each component are performed in Section 6 by varying the design parameters in green. Rotor design parameters (orange) affect all aspects of turbine design.**Upwind vs. Downwind is duplicated**

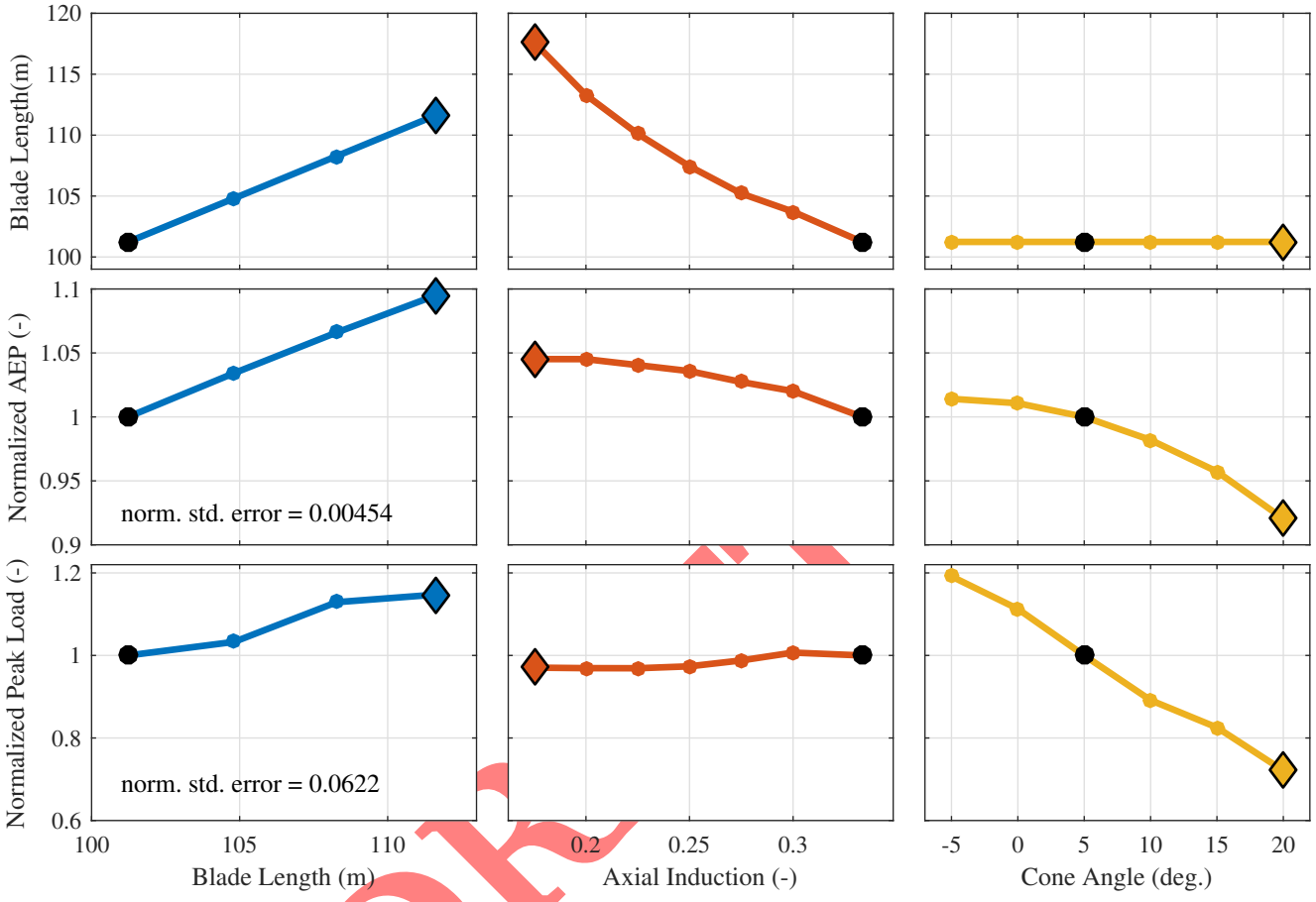

Figure 5. Summary of aerodynamic design studies: the blade length, axial induction, and cone angle are varied while the AEP and peak blade load are calculated and compared to the base case (SUMR-13A). The standard deviations of the errors for AEP and peak flapwise load are normalized to the SUMR-13A values and apply across all design studies.

loads. In the most extreme example, a blade with a 0.175 axial induction factor can increase the AEP by 5% over a rotor with aerodynamically optimal blades (axial induction factor of ⅓), but requires 16% longer blades.

The cone angle design study was performed using the same baseline SUMR-13A rotor, but with a varied cone angle, including upwind (negative) cone angles. Downwind, highly coned rotors decrease the rotor swept area, resulting in lower power capture and blade loads. The load decrease is significant: 25% compared with a 7% decrease in power capture. In comparison with the length design study, it is clear why highly coned rotors are attractive for large rotor designs: an increased cone angle will decrease loads faster than an increase in blade length will increase them.

For all the aerodynamic design studies, there is a trade-off between power capture and blade root loading. Each design study is plotted together in Fig. 6; it also includes DELs in the flapwise and edgewise direction. In rotor design, our goal is to maximize AEP and decrease blade loads, providing results in the lower-right quadrant of each plot. The design changes can

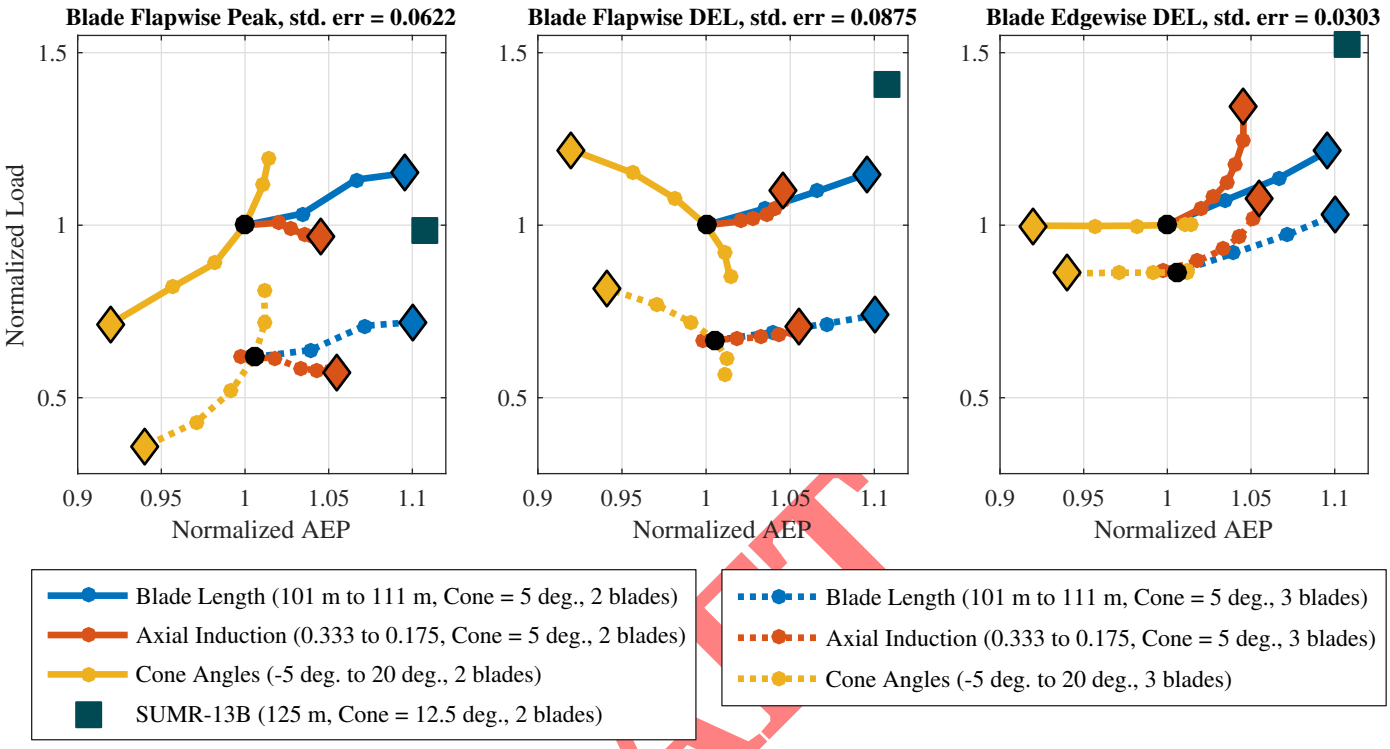

Figure 6. The trade off between power capture and blade loads. The AEP is plotted on the x-axis and blade loads are plotted on the y-axis. Both are normalized to the 2-bladed 101 m SUMR-13A baseline rotor design. Each dot represents a rotor design and each line represents a design study. The normalized error standard deviation for AEP is the same as in Fig. 5 and the load error is normalized to the SUMR-13A loads.

also be applied in combination, as illustrated by the SUMR-13B, which was designed starting from the longest blade length, used an axial induction of 0.2, and a cone angle of 12.5 deg. The SUMR-13B increases AEP by 11%, compared to the SUMR-13A, while constraining peak blade loads. The increased blade length increases the flapwise DELs due to the enhanced effect of wind shear and edgewise DELs are increased due to the additional blade weight.

Three-bladed rotors were designed similarly to the two-bladed design studies (shown with dotted lines in Fig. 6) and exhibit similar trends to the two-bladed rotors in terms of blade loads. The three-bladed rotors have lower loads with the same power capture due to their smaller chord and mass.

Despite the larger blade loads on 2-bladed rotors compared to 3-bladed rotors with the same power capture, we will be analyzing the 2-bladed SUMR-13B for the remainder of this study. Comparing similarly sized rotors, e.g. the CONR-13 and the SUMR-13A, 2-bladed rotors reduce the total blade mass by as much as 25%, which reduces the capital expenditures associated with blade material costs. There are also cost benefits in manufacturing and transportation (Griffith, 2017). The larger chord lengths of 2-bladed rotors increase the edgewise stiffness, leading to greater aeroelastic stability in terms of classical flutter (Griffith and Chetan, 2018). However, periodic effects are more pronounced on the non-rotating components

of 2-bladed rotors. We will analyze the load alleviating potential of different hub configurations in Section 6.3 and structural reinforcement in Section 6.2.

6.2 Blade Structural Parameters

A a wind turbine blade increases in length, its mass and stiffness increase to account for the additional structural loading. The structural properties of a blade are described by its distributed parameters along the blade span, which include mass-, stiffness-, and inertia-per-unit-length. In the previous section, these distributed structural parameters were constant for different blade lengths. Here, we will examine the effect of changing these parameters and, later, choose design parameters sufficient for a larger blade. To model blades with different lengths, we start with classical similarity scaling rules, based on the length scaling factor

$$\eta = L/L_0, \tag{14}$$

where L is the length of the scaled blade and L_0 is the length of the original blade. In this study, L_0 is the length of the baseline blades: the SUMR-13A for 2-bladed rotors and the CONR-13 for 3-bladed rotors. We will examine the scaling of the following parameters (Griffith and Ashwill, 2011):

- mass per-unit-length, which scales with η^2
- stiffness per-unit-length in the flapwise, edgewise and torsional directions, which scales with η^4
- stiffness per-unit-length in the spanwise direction, which scales with η^2, and
- inertia per-unit-length in the flapwise and edgewise directions, which scales with η^4.

Once integrated over the blade length, e.g., the mass scales with η^3, while the stiffness and inertia properties scale with η^5.

These parameters can be more flexibly scaled to account for innovations or changes to the structural design. For instance, we scale the mass-per-unit-length by

$$m(r) = m_0(r)\eta^{2k_M}, \tag{15}$$

where $m(r)$ is mass-per-unit-length at spanwise location r of the scaled blade, m_0 is the mass-per-unit-length of the original blade, and k_M is a tunable parameter to increase or decrease the blade mass. Based on (15), a $k_M = 0$ would produce a blade with a mass that scales linearly with blade length, while $k_M = 1$ would produce a blade with a mass that scales with the cube of blade length. State-of-the-art trends show that mass scales roughly to the square of blade length, or $k_M = 0.5$. A similar parameter can be defined for stiffness scaling

$$k_{s,flap} = k_{s,flap,0}\eta^{4k_{Fs}}, \tag{16}$$

where $k_{s,flap}$ is the flapwise stiffess-per-unit-length of the scaled blade, $k_{s,flap,0}$ is the flapwise stiffess-per-unit-length of the original blade and k_{Fs} is a tunable flapwise scaling parameter. The edgewise stiffness will be similarly scaled using a

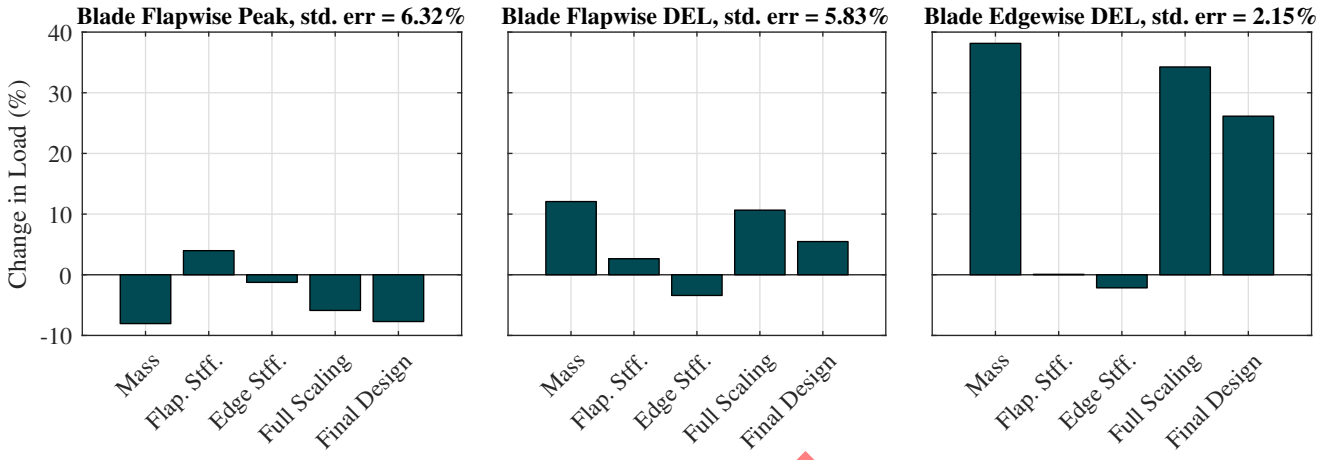

Figure 7. The effect of mass scaling ($k_M = 1$), flapwise stiffness scaling ($k_{Fs} = 1$), edgewise stiffness scaling ($k_{Es} = 1$), and the scaling of all parameters ($k_{\text{All}} = 1$) on blade loading compared with the non-scaled SUMR-13B ($k_{\text{All}} = 0$, the SUMR-13B loads in Fig. 6).

parameter k_{Es}. Flapwise and edgewise inertia will scale using the same mass scaling parameter k_M, but to the 4th power as in (16). Torsional and spanwise stiffness will scale according to the similarity scaling rules defined above, with no additional tuning parameter. The SUMR-13B (2-bladed, $\eta = 1.24$) structural properties were scaled from the SUMR-13A blade, first separately each for the mass and stiffness parameters, and then all together (Full Scaling) in Fig. 7.

Ultimately the final structural parameters will be determined by the structural layup, but this model could be used to more quickly analyze trade-offs between blade mass, stiffness, loads, and power. In general, mass scaling has the greatest impact on loads, especially considering fatigue loading, which experiences a fully reversing load cycle during each rotor revolution. Increased flapwise stiffness contributes to a small increase in energy capture (about 1%, not shown) due to the decreased blade deflection. We also observe that the change in load due to each individual scaling parameter (k_M, k_{Fs}, and k_{Es}) approximately sum (or combine linearly), when multiple parameters are simultaneously scaled. This is shown in Fig. 7: when summing the change in load due to Mass, Flap. Stff., and Edge Stff., is is approximately equal to the change in load due to Full Scaling. The same is true for the Final Design, which is a combination of the scaling parameters that are determined in the next section.

6.2.1 Selecting a k_M and k_{Es} for Edgewise Fatigue Loads

The most significant impact of structural scaling is the increase in edgewise DELs due to the increased blade mass. Theoretically, the additional mass increase of the larger blade would provide additional reinforcement against these loads, through trailing edge reinforcement or increased root diameter. We see that changes to the blade mass impact the edgewise loads, i.e.,

$$\delta M_{bx} = a_1 k_M + b_1, \tag{17}$$

Table 3. Blade structural coefficients for the SUMR-13B blade.

Structural Relations		Final Design Coefficients
$a_1 = 0.51,$	$b_1 = 1.40$	$\delta M_{bx} = 1.8$
$a_2 = 0.95,$	$b_3 = -0.79$	$k_{Es} = 0.92$
$a_3 = 0.87,$	$b_2 = 0$	$k_M = 0.804$

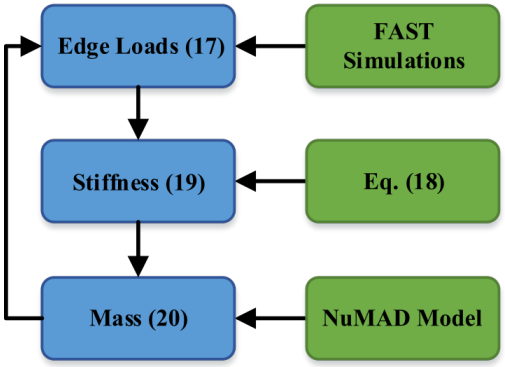

Figure 8. The relationship between blade mass, edgewise loads, and edgewise stiffness, as well how each value was derived.

where a_1 and b_1 are determined from FAST simulations of the SUMR-13B blade with multiple k_M values from 0 to 1. Additional edgewise stiffness must compensate for the increase in edgewise load by increasing the ultimate load

$$M_{ult} = \frac{2\sigma EI_x}{c}, \tag{18}$$

where σ is the fiberglass strain limit at the trailing edge, EI_x is the edgewise stiffness, and c is the blade chord. In terms of the scaling coefficients, a linearized version of (18) can be obtained

$$k_{Es} = a_2 \delta M_{bx} + b_2. \tag{19}$$

Finally, changes to the blade structural layup in the form of trailing edge reinforcement to increase edgewise stiffness will increase the blade mass

$$k_M = a_3 k_{Es} + b_3, \tag{20}$$

where a_3 and b_3 are determined by designing multiple blades in NuMAD with a target k_{Es} from 0 to 1. Additional trailing edge reinforcement was applied to meet the target values within 5% and the k_M was computed using the overall mass of the resulting blade model.

The linear system determined by (17), (19), and (20) can be solved to determine the necessary structural reinforcement for accommodating the load increase due to the increase in mass. See Table 3 for details. Eventually an optimized SUMR-13B structural layup will be designed to also account for nonlinear effects like buckling and classical flutter. For the remainder of this study, we will evaluate the loading on other components as a result of the mass increase determined here.

6.3 Hub Configuration

The additional blade mass associated with larger blades will result in larger loads on non-rotating turbine components. Different hub configurations can alleviate these loads. Here, we will analyze the difference between 2- and 3-bladed rotors on main

Table 4. Comparison of the steady-state (8.5 m/s) hub load harmonics for 2-bladed fixed, teeter, and IPC configurations, as well as 3-bladed rotors, in upwind and downwind positions. We analyze the cosine-cyclic hub load in the y-direction (m^1_{hy}, Fig. 3) and the sine-cyclic hub load in the z-direction (m^1_{hz}) because of their combined effect on non-rotating component loads. The different teeter and IPC configurations are presented in Section 6.3.2.

Rotor Location	Hub Configuration	Rotor Model	$m^{1P}_{hy,c}$	$m^{1P}_{hz,s}$
Downwind Rotors	2-bladed Fixed Hub	SUMR-13A	15500	-8840
		SUMR-13B	22500	-16200
	2-bladed Teeter	Free Teeter	0	-16900
		Opt. Teeter	16200	-16400
	2-bladed IPC	Opt. Blade	10800	-11200
		Opt. Main Br.	-17700	-16200
	3-bladed Fixed Hub	SUMR-13A (3b)	7180	-7220
		SUMR-13B	24900	-24700
Upwind Rotors	2-bladed Fixed Hub	SUMR-13A	3780	-3570
	3-bladed Fixed Hub	SUMR-13A (3b)	-526	543

bearing loads. For 2-bladed turbines, we observe load increases for which we deign teeter hinges and individual pitch controllers in order to alleviate the loading on the main bearing. Also, we investigate the effect of large cone angles on the peak load of the main bearing since, intuitively, we expect to see a significant increase for downwind rotors. The different hub configurations explored in this section transfer the loads from the blades to the hub in different ways, affecting the main bearing and other non-rotating components differently.

6.3.1 Number of Blades

To compare with the 2-bladed SUMR-13B, a 3-bladed SUMR-13B was designed using the same blade parameters described in the previous sections. The additional blade increases AEP by about 8% (Fig. 9, left). The increased power capture causes the rated wind speed to occur at a lower wind speed, slightly reducing peak loads through pitch control. DELs in the flapwise and edgewise directions of the blades are unaffected by the change in the number of blades, which implies that the same blades would pass the same structural strain limits, possibly with more tolerance.

Loads on other components of the turbine are, however, affected by the change in the number of blades. Hub loads on the 2-bladed SUMR-13B are mostly in the y-direction (see $m^{1P}_{hy,c}$ in Table 4), while the 3-bladed rotors are balanced in both directions due to rotor symmetry. The effect of these hub loads is most apparent when analyzing the loading on the non-rotating main bearing. The components in Table 4 can be mapped to the non-rotating frame by (11). The 1P harmonic in the rotating

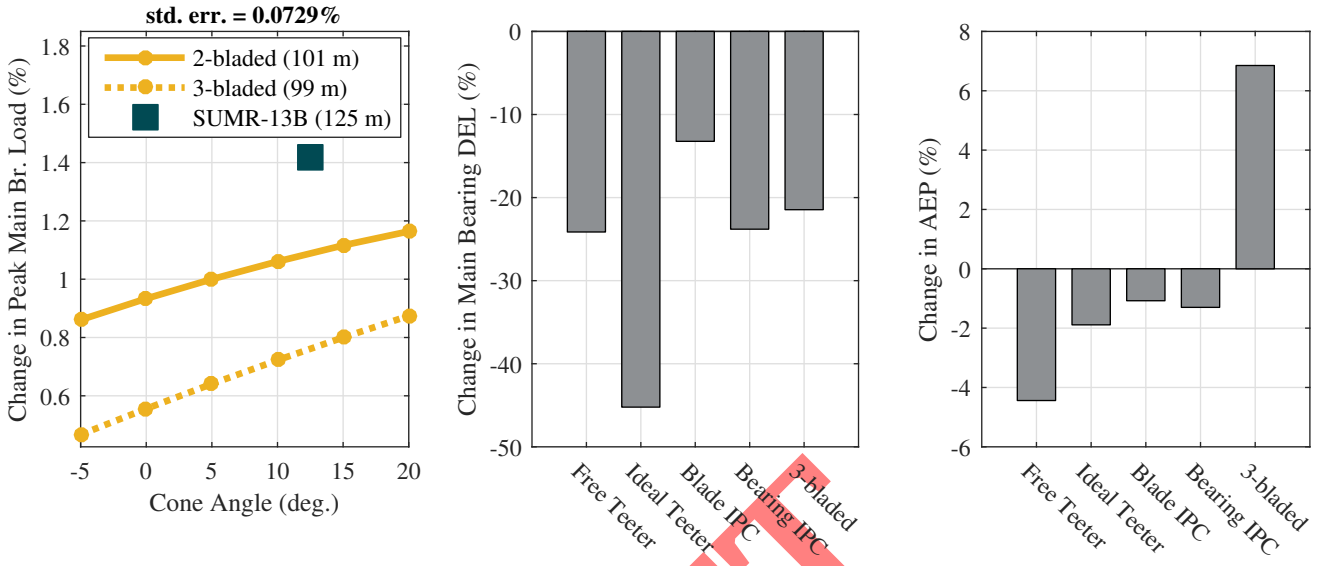

Figure 9. Peak main bearing loads (left) for SUMR-13A cone angle study (2- and 3-bladed rotors) and SUMR-13B fixed hub configuration, main bearing DELs (middle) in the y-direction (DELs in the z-direction are within 5% of the y-direction DELs) and change in AEP for different hub configurations of the SUMR-13B compared with the fixed-hub, 2-bladed SUMR-13B described in Section 6.2.1. The DEL and AEP results from different hub configurations (center and left) are design loads directly from DLC simulations.

frame transfers to 0P and 2P harmonics according to

$$m_{hy}^{0P} = \tfrac{1}{2}(m_{hy,c}^{1P} - m_{hz,s}^{1P}) \tag{21}$$

$$m_{hy}^{2P} = \tfrac{1}{2}(m_{hy,c}^{1P} + m_{hz,s}^{1P}). \tag{22}$$

The 3P component is determined similarly based on the 2P harmonic load components.

Three-bladed rotors are advantageous due to these balanced hub loads, which effectively nullify the 2P load components and only contain a small 3P load on the non-rotating turbine components. The difference in magnitude of 1P hub load harmonics is responsible for the greater loading on the non-rotating components of 2-bladed rotors. Fig. 9 shows more than a 20% reduction in main bearing DEL for the 3-bladed SUMR-13B, compared to the 2-bladed SUMR-13B, even with a significantly more powerful rotor.

6.3.2 Teeter and Individual Pitch Control

Historically, 2-bladed turbines have used a mechanical teeter hinge, which allows for rotation about an axis perpendicular to the main shaft at the shaft tip. Recently, with the advent of pitch regulated turbines, individual pitch controllers have been designed in order to mimic this action by changing the aerodynamic loads on the blades as they rotate. Both solutions reduce loading on the hub, which translates into reduced loading on the main bearing and other non-rotating components.

We have modeled a free teeter hinge in FAST by enabling the teeter degree-of-freedom and setting a zero damping coefficient to the teeter motion. This free teeter setup would provide the best configuration for reducing blades loads. A more realistic teeter hinge must account for the friction, damping, and end stops (see, e.g., Schorbach et al. (2017)).

The free teeter hinge configuration completely eliminates the coupling between blade loads and eliminates the hub loads in the y-direction (Table 4). The relationship in (22) and steady-state results suggest that main bearing loads actually increase when compared to the fixed hub configuration. However, turbulent simulations show that turbulence has a relatively minimal impact on the non-rotating components for the free teeter configuration when compared with all the other rotors. In other words, the design loads for the main bearing are nearly equal to the steady-state loads, but in every other case there is a significant turbulent component; this will be discussed in Section 7. For this reason, it will be omitted from the calibration set of 2-bladed rotors. Instead of presenting the calibrated DEL in the middle and right of Fig. 9, we show the actual design load from DLC simulations. The steady-state results in Table 4 still illustrate how a more optimal teeter design might mimic the balanced hub loads of 3-bladed rotors.

A more optimal teeter design could be achieved by selecting the appropriate teeter damping coefficient d_{teet} that matches the $m^{\text{1P}}_{hy,c}$ and $m^{\text{1P}}_{hz,s}$ load harmonics to minimize the main bearing load m^{2P}_{my}. Since only one damping coefficient must be designed for all wind speeds, we minimize the main bearing load using the wind speed distribution $p(u)$ by

$$d_{\text{teet,opt}} = \underset{d_{\text{teet}}}{\arg\min} \sum_{u \in U_{\text{teet}}} p(u) m^{\text{2P}}_{my}, \tag{23}$$

where U_{teet} is the set of wind speeds used to analyze the teeter damping, focused on below-rated operation, where the greatest fatigue contribution occurs. The ideal teeter design greatly reduces the main bearing DELs, along with the DELs on the rest of the stationary components, at the cost of a 1.9% power loss (compared with the fixed 2-bladed SUMR-13B).

Alternatively, individual pitch control (IPC) can be used to mimic the rotor balancing of a teeter hinge by adding a pitch angle offset to each blade. An IPC control was initially designed to focus on blade loads, which we call Blade IPC in Table 4 and Fig. 9. The 2-bladed IPC architecture used here was initially presented in van Solingen and van Wingerden (2015), which minimizes the teeter load

$$m_{\text{teet}} = \frac{1}{2}(m_{by,1} - m_{by,2}). \tag{24}$$

We have applied loop-shaping procedures (McFarlane and Glover, 1992) to fine tune the controller to reduce the 1P and 2P blade harmonics, which results in a decrease in the blade design load for the SUMR-13B (about 10% for flapwise peak and fatigue loads). The IPC controller was designed to operate both above- and below-rated, since the bulk of the fatigue loads occur below rated, and the IPC controller must be active near rated in order to reduce the peak design load. Since the Blade IPC controller is designed to reduce blade loads as much as possible, hub loads in the y-direction are less than hub loads in the z-direction (Table 4). Therefore, the Blade IPC controller is not necessarily optimal for the main bearing DELs.

By directly targeting the difference in the components of (22), we designed a Bearing IPC controller, which better balances the load hub load components (Table 4) and reduces main bearing DELs during turbulent simulations (Fig. 9). To properly balance the hub loads and minimize non-rotating loads, m_{hy} and m_{hz} should be equal in magnitude and 90° out of phase.

Since m_{hz}^{1P} changes slower than m_{hy}^{1P}, the m_{hz} signal is delayed by 90° and the difference

$$m_d = m_{hy} - m_{hz}(\psi - 90°) \tag{25}$$

can be fed back using the same architecture as the Blade IPC controller because $m_{hy} = 2m_{\text{teet}}$. Steady-state results suggest better load mitigation than those in Fig. 9. So, the design DELs from turbulent simulations are presented here. In general, dynamic control solutions are not well estimated using the harmonic load model presented in this paper, compared with changes to the rotor model using the same control.

Other methods were attempted to balance the load components in (22). Direct calculation of the components from (5) and (6) requires at least one period of load information, which introduces excessive time lag during turbulent simulations. Alternatively, the load components can be estimated using the multi-blade coordinate transform (Bir, 2008), but notch filters must be used at the 2P and 4P harmonics to avoid unnecessary pitch action. As rotors increase in size, the rated rotor speed slows, resulting in a combination of larger load components and lower frequencies. The filters necessary for adequate control signals for cyclic pitch control also result in unsatisfactory time lag.

If used below rated, these load mitigation techniques reduce power capture, as shown in the right of Fig. 9. IPC is typically designed so that it only operates above rated, resulting in a negligible power loss. However, this reduces its effectiveness in constraining peak loads that occur close to rated wind speeds.

6.3.3 Large Cone Angle Effects

The steady-state results in Table 4 suggest a major difference between the m_{my}^{0P} of upwind and downwind turbines. Intuitively, we can see that the non-rotating moment at the hub will be larger because the moment due to wind shear and gravity are in the same direction for downwind turbines, whereas for upwind turbines they are in the opposite directions and cancel. We analyze the effect of cone angle on the peak main bearing moment ($m_{my}^{0P} + m_{my}^{1P}$) in the y-direction (Fig. 9, left).

The steady-state results suggest there would be a large change (about 5 times) in mean main bearing load going from upwind to downwind turbines. However, the design loads computed in turbulent DLC simulations show that turbulence contributes a large amount to the peak load experienced by the main bearing. We will discuss the details in Section 7. Calibrated peak loads are shown in Fig. 9 and are subject to a non-negligible error.

A downwind configuration, compared to the same rotor upwind, only increases the main bearing load by about 15%. Despite the larger total blade mass of the 3-bladed rotors, 2-bladed rotors still have a larger peak load due to unsteady effects and a larger turbulent load component. We see this same effect in the DEL values of Fig. 9, suggesting that main bearing peak loads could be reduced by using the same methods we just discussed. The SUMR-13B peak main bearing load has a non-negligible increase due to combined increases in blade mass, unsteady effects due to increased blade length, and a larger cone angle. These increased loads on the main bearing transfer to the other non-rotating components, which we will analyze in the following design studies.

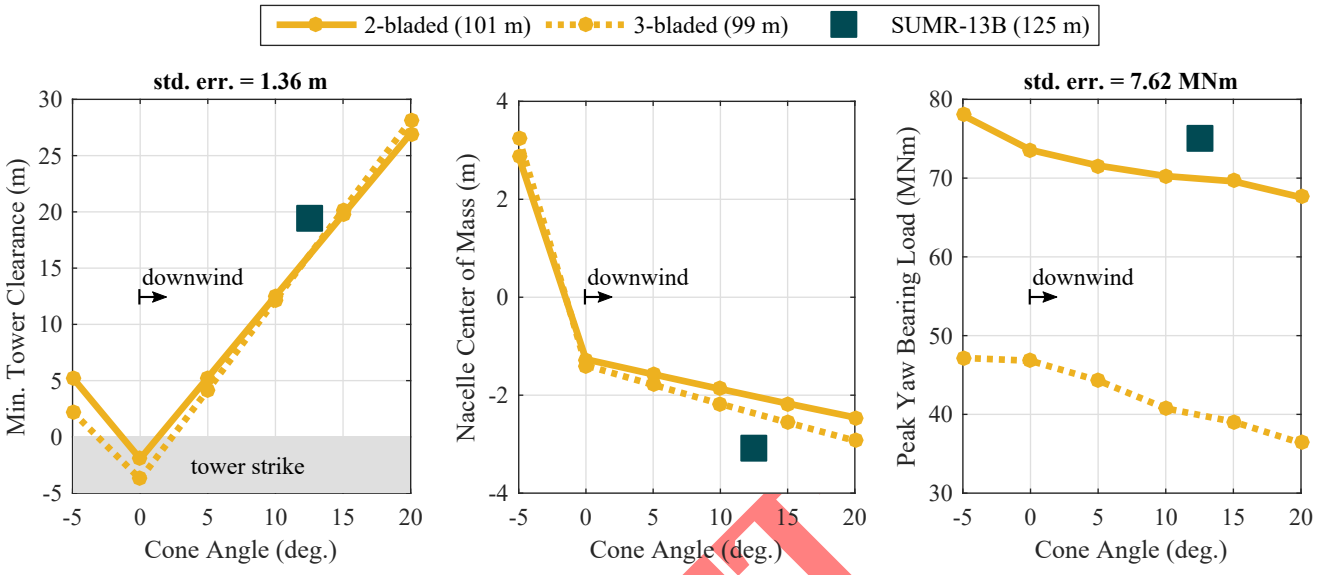

Figure 10. The tower clearance (left) resulting from upwind and downwind configurations, the nacelle center of mass (middle) required to balance rotor on a 13 MW coned rotor, and the peak yaw bearing loads (right) of the balanced, coned rotors.

6.4 Nacelle Layout

Since the loading on the yaw bearing and main bearing are similar, it is expected that downwind turbines would experience large peak overturning moments on the yaw bearing, like those seen on the main bearing. However, peak loads on the yaw bearing can be counteracted by properly balancing the nacelle on the tower. We will study the different cone angle designs from Section 6.1 for 2- and 3-bladed rotors, as well as our SUMR-13B design choice to investigate the effect of rotor cone angle and mass on nacelle design and yaw bearing loads.

A large mean overturning moment (m_{yy}^{0P}) on the yaw bearing causes large peak loads that can be overcome by properly choosing the hub-to-tower overhang and the nacelle center of mass. We will use a simple solution to designing the nacelle overhang: for upwind turbines, the nacelle overhang was set to that of the CONR-13 (-8.61 m), and for downwind turbines, we used the minimum possible overhang (3.15 m, equal to the radius of the tower at the nacelle). These overhang designs result in adequate tower clearance values when the cone angle is at least 5° in either direction (Fig. 10, left). Rotors with larger cone angles have substantial tower clearance, which is part of the motivation for their design.

Next, we designed the nacelle center of mass x_{cm} so that the mean yaw load was minimized in 0 m/s wind, i.e.,

$$x_{cm} = \arg\min_{x_{cm}} |m_{yy}^{0P}|. \tag{26}$$

Since the relation between the mean overturning yaw bearing load is straightforward and linearly dependent on the component masses and center-of-masses

$$m_{yy}^{0P} = g(m_{\text{nac}} x_{cm} + m_{\text{rot}} x_{cm,\text{rot}}), \tag{27}$$

Table 5. Component masses for centering nacelle on tower.

Component	Mass (Mg)
Nacelle	1030
Hub	245
Blade (2-bladed SUMR-13A)	51.8
Blade (3-bladed SUMR-13A)	47.3
Blade (2-bladed SUMR-13B)	83.8

where g is the acceleration due to gravity, m_{nac} is the nacelle mass, m_{rot} is the total rotor mass, including the hub (Table 5), and $x_{cm,\text{rot}}$ is the rotor center of mass. The nacelle center of mass that minimizes the mean overturning yaw bearing load is

$$x_{cm} = -\frac{m_{\text{rot}} x_{cm,\text{rot}}}{m_{\text{nac}}}. \tag{28}$$

The rotor mass m_{rot} is the sum of the total blade and hub mass, while the nacelle mass m_{nac} is scaled up from the NREL 5 MW reference turbine (Jonkman et al., 2009), shown in Table 5. The hub and nacelle masses are constant for all rotors throughout this study.

To balance a turbine, rotors with large downwind cone angles must have center of masses further upwind (Fig. 10, center). With the nacelle mass in Table 5, moving the nacelle center of mass 1 m upwind reduces the mean (and peak) yaw moment by about 10 MNm. Due to the extra overhang necessary for upwind turbines, the center of mass location for the downwind turbines is closer to the tower than for the upwind turbines. By designing the proper hub to tower overhang and nacelle placement, the peak yaw load are no more problematic for downwind rotors than upwind rotors. Once properly balanced, the peak yaw loads are primarily driven by the thrust imbalance due to wind shear, which decreases with increased cone angle (Fig. 10, right). Fatigue loads (not shown) on the yaw bearing also depend on rotor thrust and decrease with increasing cone angle. The methods presented in Section 6.3 also reduce yaw bearing loads. Additionally, a downwind turbine could be designed to yaw freely to reduce blade and yaw bearing loads (van Solingen et al., 2016).

6.5 Tower Design

The final turbine component we will analyze for different rotor design choices is the largest one: the tower. The tower experiences large peak loads in the fore-aft direction m_{ty} and large damage equivalent loads in both the fore-aft and side-to-side (m_{tx}) directions.

The peak loads experienced by the tower are similar to the blade loads shown in Section 6.1; they are largely driven by rotor thrust. The mean fore-aft load $m_{ty}^{0\text{P}}$ is most sensitive to axial induction and cone angle, since both alter the rotor thrust. Lower axial induction rotors and downwind rotors can both reduce the peak tower load by as much as 20% (Fig. 11, left). Tower loads are not as sensitive to blade length. Longer blades increase the rotor thrust at below-rated wind speeds, but with a constant generator power, the pitch controller activates at lower wind speeds, constraining the peak tower load near rated. For rotors that

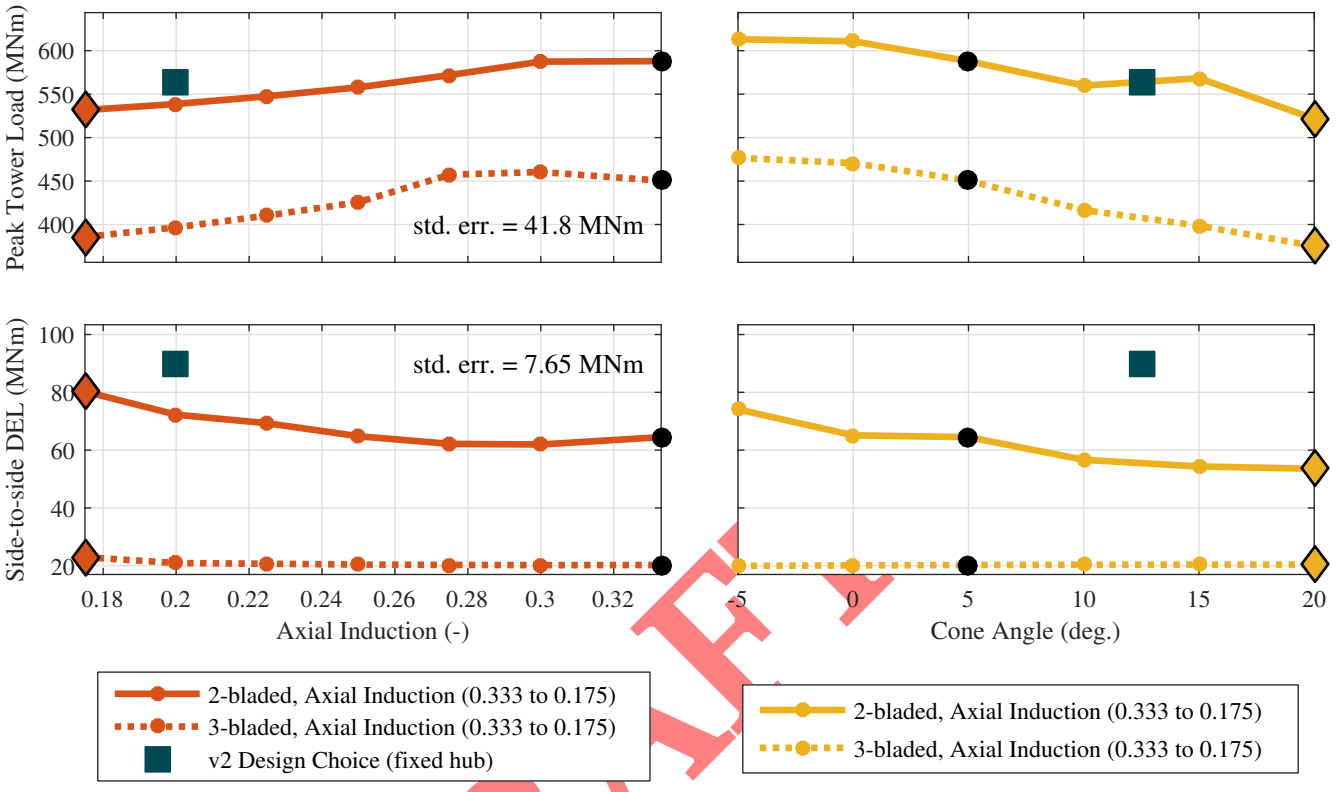

Figure 11. Peak tower loads (fore-aft, m_{ty}^{peak}) and side-to-side DELs (m_{tx}^{DEL}) for rotors with different axial induction factors (red), cone angles (yellow), and number of blades. The same loads for the v2 design choice are also shown. The standard deviation of error for both loads are across all design studies.

capture the same amount of power, 2-bladed rotors experience about a 30% increase in peak load when compared to 3-bladed rotors, primarily due to a large difference in the turbulent sampling of the wind, an effect also present when looking at the tower DELs.

Besides having larger chord lengths that sample more turbulence than 3-bladed rotors, 2-bladed rotors also experience a resonance due to the tower design. When the 2P rotor speed interacts with the natural frequency of the tower, there exist high fore-aft and side-to-side loads. The side-to-side DELs are increased the most, since there is little aerodynamic damping from the rotor in this direction. Our solution is to implement a speed avoidance controller that slows down the rotor speed before the critical rotor speed and speeds it up after, avoiding the critical speed as much as possible (Fig. 12, center). While this controller does reduce the side-to-side loading, 2-bladed rotors still experience nearly 2 times the DELs that similar 3-bladed rotors experience (Fig. 11). Changing hub architectures also impacts the tower DELs. Both teeter and IPC decrease the fore-aft loading while increasing the side-to-side loading.

Our results suggest that downwind, coned rotors are not problematic for tower loading; they actually reduce tower loads. However, 2-bladed rotors are problematic for traditional tower designs. Control solutions can help, but the tower loads are still significantly higher, which may motivate the use of floating towers with very low natural frequencies for 2-bladed rotors.

Our steady-state simulations predict the same peak tower loads for both 2- and 3-bladed rotors, but turbulent simulations suggest a clear difference in the design load. Hence, the calibrated peak loads shown in Fig. 11 represent this difference. Estimated tower loads display a large amount of uncertainty (Fig. 14) when compared with turbulent DLC simulations. This uncertainty can be attributed to the nature of these tower loads, which are highly dependent on turbulent gusts, where control schemes can have the greatest impact, especially when switching from below to above-rated operation.

6.6 Closed-loop Control

Every rotor in this study has been simulated with closed-loop control. In below-rated conditions, the generator torque is controlled so that the rotor speed is optimal for power capture, following the typical $\tau_g = k\omega_g^2$ law for most of the below-rated operating region, before transitioning to above rated. For simplicity, this is implemented as a look-up table, though more sophisticated methods exist. The look-up table is altered to avoid the critical rotor speed for 2-bladed rotors only (see Fig. 12, center). In above-rated wind speeds, the pitch angle is controlled to regulate the rotor speed to its rated value using a gain-scheduled proportional-integrator (PI) control. The gains of the PI control are set so that pitch travel is minimized, subject to a constraint on the maximum generator speed. We have chosen this simplified control architecture so that it can be easily tuned for a large number of rotors in the same way. The optimal gain k is computed using rotor parameters and the PI control gains are tuned using a subset of the DLC 1.2 turbulent simulations (Zalkind et al., 2017). The controller we have implemented here is based on the NREL-5MW baseline controller (Jonkman et al., 2009); it is commonly used as a reference to compare new controller designs and is similar to industry standard control. This baseline control is not necessarily the best controller possible, but it allows us to adequately analyze power and load sensitivity to model changes.

Implementing a controller for steady-state simulations allows us to incorporate the transition from below- to above-rated operation, giving us a more accurate representation of the peak loads that occur near rated wind speed. With a constant generator size (13.2 MW), different rotors transition from below to above rated at different wind speeds, which is modeled in steady state. Additional control signals, like individual pitch control (IPC) signals are added to the baseline control signals described above. The power losses associated with IPC below rated can be observed in steady-state simulations.

A controller is necessary for computing the design load in turbulent DLC simulations. Non-uniform wind shear and wind speed changes, or gusts, need to be adequately controlled. One particular case causes many of the peak component loads, which we show in Fig. 13. During a decrease in wind speed, the rotor slows and the pitch decreases to its optimal power position. When the decrease in wind speed is followed by a positive gust, the pitch control must react quickly to regulate rotor speed. Sometimes the actuator limits are too slow to react to the positive gust. We have modeled the actuator of each rotor in this study as a 2$^{\text{nd}}$-order Butterworth filter with a cut-off frequency of 0.25 Hz. This decrease and then increase in wind speed creates a condition where there is an above-rated wind speed, but a below-rated pitch angle, resulting in an increased thrust on the rotor and high loads.

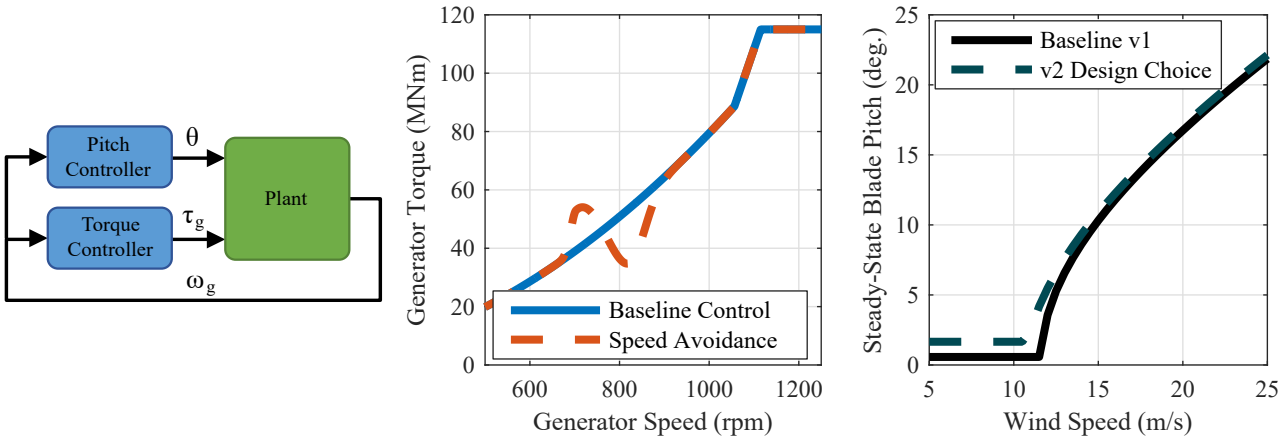

Figure 12. Baseline control block diagram, where θ is the pitch angle, τ_g is the generator torque, and ω_g is the measured generator speed (left). The torque control signal (center) for baseline control (blue) and speed avoidance control (red). Steady-state blade pitch angles for the SUMR-13A and SUMR-13B.

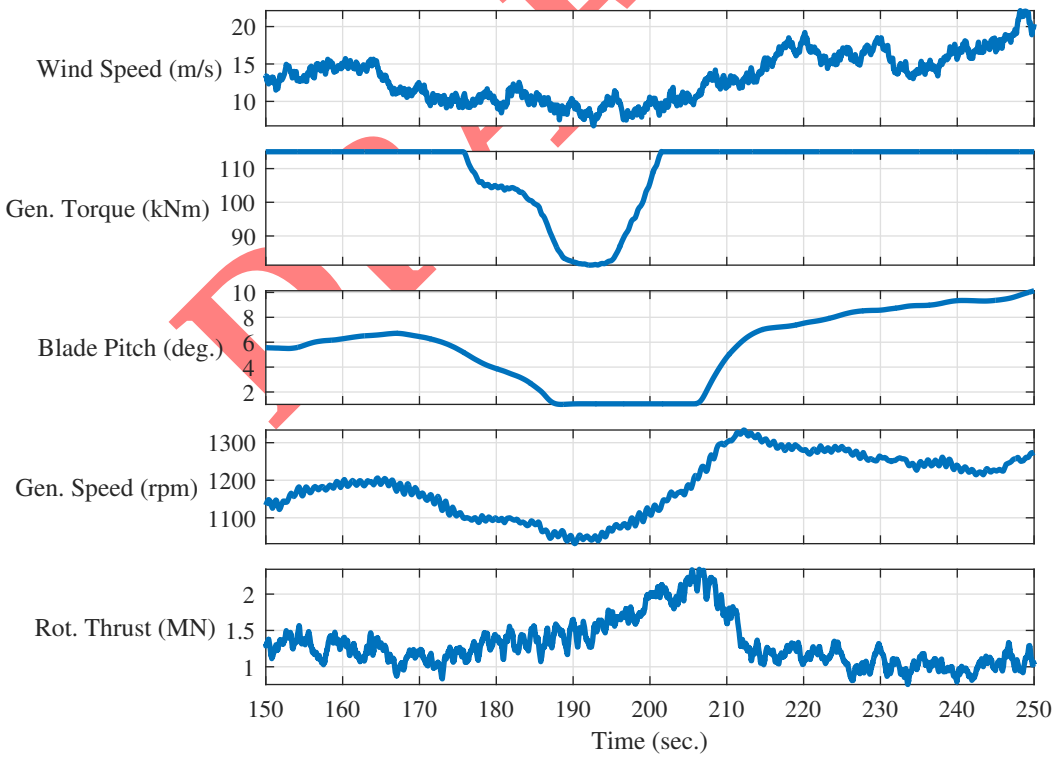

Figure 13. Baseline control illustration of a problematic gust for SUMR-13A baseline rotor in extreme turbulence (DLC 1.3) with a mean wind speed of 14 m/s. The peak rotor thrust near 205 sec. caused the greatest load in all DLC simulations; it causes the peak blade flapwise load for the SUMR-13A.

These problematic gusts and turbulence are what drive the design load for components using DLC simulations. The effects are partially inherent in the steady-state model, by modeling the peak loads, but uncertainty does exist due to closed-loop control and at other places in the model, which we describe next.

7 Model Calibration and Uncertainty

The data presented to this point has been from steady-state results that are calibrated to the design loads computed in DLC simulations. To compute these design loads, we simulated the power producing DLCs specified by the IEC standard:

- DLC 1.2: normal turbulence, for fatigue loads, using 6 random seeds at mean wind speeds from cut-in to cut-out, spaced 2 m/s apart
- DLC 1.3: extreme turbulence, for peak loads, using the same number of turbulent wind seeds and wind speeds
- DLC 1.4: extreme coherent gust with direction change, for peak loads near rated, above- and below-rated wind conditions. Different rotor azimuthal initial conditions were simulated to account for the rotor being in different positions when the gust occurs.
- DLC 1.5: extreme wind shear, for peak loads near rated and at cut-out wind speeds. The same azimuthal initial conditions were used as DLC 1.4.

In this section we will present a comparative analysis of the steady-state harmonic loads and the loads computed in DLC simulations, a method for calibrating the steady-state loads to more accurately estimate the design loads, and an analysis of the uncertainty present in the calibrated loads. Instead of simulating every rotor presented thus far (45 rotors), we have chosen a smaller subset to analyze and calibrate the harmonic model:

- CONR-13, SUMR-13A, and SUMR-13B with fixed hub, free and optimal teeter, blade and main bearing IPC, and 3-bladed configurations
- the 2- and 3-bladed aerodynamic trade study endpoints: greatest blade length, axial induction, and cone angle change (including upwind).

The design loads of the free teeter hinge will not be included in the calibration and uncertainty analysis for reasons described in Section 6.3.2; it is marked with an ‘x’ in Fig. 14.

In Fig. 14 (top, left) we show the steady-state harmonic loading and the design load for the peak main bearing load. In general, the load due to the steady-state harmonics is much less than the design load. For each component, part of the load can be attributed to the steady loading and part to the turbulent loading:

$$m^{\text{DLC}} = m^{\text{SS}} + m^{\text{turb}}. \tag{29}$$

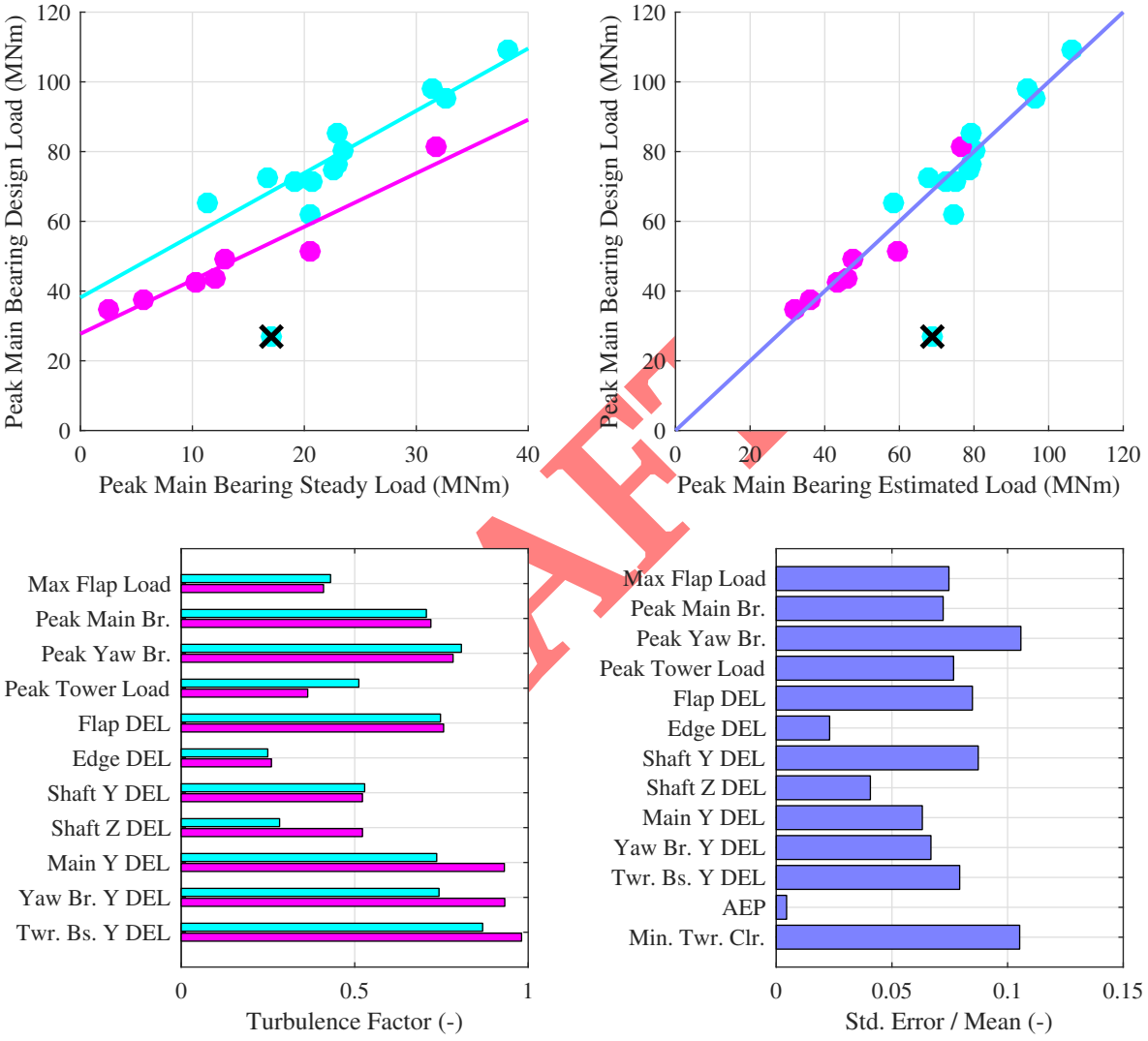

Figure 14. Peak main bearing loads computed using the steady-state harmonic model versus the design load (top, left) and calibrated load estimates (top, right) for two-bladed rotors (cyan) and three-bladed rotors (magenta). The same color scheme is used to show the relative effect of turbulence on selected component loads (bottom, left), as defined in (30), and the standard deviation of the error normalized by the mean load is shown for the whole calibration set (bottom, right).

We quantify the turbulent load contribution of each component load using the turbulence factor

$$f^{\text{turb}} = \frac{\text{mean}(m^{\text{turb}})}{\text{mean}(m^{\text{DLC}})}. \tag{30}$$

Fig. 14 (left, bottom) shows the turbulence factor for a selection of the component loads. Some loads, like the edgewise DEL and the shaft DEL in the z-direction for 2-bladed rotors are more deterministic, with a lower turbulent component, than the others. In general, peak loads are more deterministic than DELs and rotating component loads are more deterministic than non-rotating component loads. We also see a difference in how turbulence affects 2- vs. 3-bladed rotors, illustrated by the different lines of fit in Fig. 14 (top, left). In general, for thrust driven loads, 2-bladed rotors have a greater turbulent load component; they also have a larger steady component, so the turbulence factor is largely consistent with 3-bladed rotors. For 3-bladed rotors, the non-rotating load component DELs are not clearly modeled by their steady-state harmonic load, so they have a relatively high turbulence factor. Even with large turbulent components that are not directly modeled in steady state, there is still good correlation with the steady loads.

We have calibrated the steady-state harmonic loads by fitting a linear model through the steady state and design loads

$$m^{DLC} = am^{SS} + b \tag{31}$$

using a linear least squares estimate of the parameters a and b. Because 2- and 3-bladed rotors sample turbulence differently, we have a set (a, b) defined for each, illustrated in the different fits in Fig. 14 (top, left). To estimate the design load,

$$m^{est} = am^{SS} + b, \tag{32}$$

results in an estimated load equal to the design load, plus some uncertainty (Fig. 14, top, right).

We analyze uncertainty of the calibrated data set (both the 2- and 3-bladed rotors, without the outlier case) by computing the standard deviation of the error for each component. The standard deviation of error is normalized by the mean load over all rotors and shown in Fig. 14 (bottom, right). We also indicate the standard deviation of the error for each component load in the figures of Section 6.

In general, the standard deviation of the error is 5-10% of the mean value, which indicates decent agreement between the load estimates and the DLC-computed loads. The cases with low standard deviation are the ones with the most deterministic load components, like the blade edgewise DEL and the shaft z-direction DEL. The AEP is also very well estimated by the steady-state model, which is good for power capture prediction as long as the effects of turbulence are calibrated.

The most erroneous load component is the peak yaw bearing load, which has a large turbulent component and where a subset of the calibration set (the 100 m designs) experience the same problematic gust event. These 100 m rotors have design loads that are about the same for each, despite the differences predicted by the steady-state model. The design loads for this component might be more a function of the gust event than the turbine configuration. The most erroneous measure (by this metric) is the minimum tower clearance; there is a large amount of uncertainty here, so a designer might want to consider doing turbulent simulations before deeming the tower safe from blade strike.

7.1 Model Limitations and Suggested Improvements

Several sources of uncertainty exist. The turbulent component is not only due to the number of blades on the rotor. There is a correlation between the rotor thrust (including cone angle) on the turbulent component. Highly coned rotors have a lower turbulent component than upwind, or lower coned rotors. Additionally, dynamic effects, like the problematic gust in Fig. 13 and the gust that caused erroneous peak yaw loads, are not explicitly modeled in this steady-state harmonic model. Dynamic control solutions that appear promising in steady state should be ultimately verified in turbulent simulations.

Several improvements to the steady-state harmonic model could be made. For instance, the problematic gust event just described follows a similar profile in many instances; this could be an additional simulation added to the model's set of simulations. Parked, fault, and shutdown cases typically result in the largest design loads in practice; they could be added with little computational expense. Finally the calibration procedure could be streamlined by perhaps doing a single, exemplary turbulent simulation for each case to determine the turbulent component of each load. Parked and shutdown cases often drive the design loads of wind turbine components. While outside the scope of this study, parked and shutdown load cases could be added to the model as additional simulations with relatively low computational effort.

8 Conclusions

In this paper, we have presented a steady-state harmonic model for wind turbine load estimation that was calibrated against the full set of operational design load cases, which could be used for initial system design or sensitivity analysis in wind turbine design. An overview of wind turbine loading was presented, with a focus on where and when the structural loads are greatest for large rotors. We have designed and presented 45 different rotors with the goal of reducing the levelized cost of wind energy through increased power capture. The power capture and structural loads have been analyzed for blades longer than 100 m in both upwind and downwind configurations, with 2- and 3-bladed rotors. A new design was presented, the SUMR-13B, with longer, more slender blades to align with industry trends. A series of detailed design studies was performed, with the following conclusions.

- Low axial induction rotors can capture more power while constraining blade loads using longer blades with smaller chord lengths.
- Downwind, coned rotors can significantly reduce peak blade loads, but capture less power than rotors with lower cone angles.
- As rotor size increases, due to increasing blade mass, edgewise blade loading becomes a critical design-driving load and may ultimately constrain the size of wind turbine rotors.
- 2-bladed rotors experience significantly greater non-rotating loads compared to 3-bladed rotors, unless a teeter hinge or individual pitch control is utilized. In these cases, the loading is comparable, but with a loss in power.
- Downwind, coned rotors will experience slightly larger (about 15-25%) peak main bearing loads than upwind turbines.

- Peak yaw bearing and tower loads are not problematic for downwind rotors as long as the nacelle is properly balanced on the tower.
- 2-bladed rotors will require either speed avoidance control or a different tower design to avoid resonance with the 2P frequency of the rotor.

We believe that our model has provided future wind turbine designers with a method for more quickly analyzing design trade-offs, and our design studies can serve as a reference for future large rotor design.

Data availability. The data from this study can be made available upon request.

Competing interests. The authors declare no competing interests.

Acknowledgements. The information, data, or work presented herein was funded in part by the Advanced Research Projects Agency - Energy (ARPA-E), U.S. Department of Energy, under Award Number DE-AR0000667. The views and opinions of authors expressed herein do not necessarily state or reflect those of the United States Government or any agency thereof.

References

Ananda, G. K., Bansal, S., and Selig, M. S.: Aerodynamic Design of the 13.2 MW SUMR-13i Wind Turbine Rotor, 2018 Wind Energy Symposium, https://arc.aiaa.org/doi/10.2514/6.2018-0994, 2018.

Bak, C., Zhale, F., Bitsche, R., Kim, T., Yde, A., Henriksen, L. C., Hansen, M. H., Blasques, J. P. A. A., Gaunaa, M., and Natarajan, A.: The DTU 10-MW Reference Wind Turbine, 2013.

Berg, J. and Resor, B.: Numerical manufacturing and design tool (NuMAD V2. 0) for wind turbine blades: User's guide, Tech. Rep. August, Sandia National Laboratories, 2012.

Bergami, L., Madsen, H. A., and Rasmussen, F.: A Two-Bladed Teetering Hub configuration for the DTU 10 MW RWT: loads considerations, in: EWEA. European Wind Energy Association, pp. 1–8, http://orbit.dtu.dk/ws/files/89799695/prod11395144001651.leob{_}Ewea2Bl{_}ver2.pdf, 2014.

Bertelè, M., Bottasso, C. L., Cacciola, S., Daher Adegas, F., and Delport, S.: Wind inflow observation from load harmonics, Wind Energy Science, 2, 615–640, https://doi.org/10.5194/wes-2-615-2017, https://www.wind-energ-sci.net/2/615/2017/, 2017.

Bir, G.: Multiblade Coordinate Transformation and Its Application to Wind Turbine Analysis, in: ASME Wind Energy Symposium, January, 2008.

Bortolotti, P., Bottasso, C. L., and Croce, A.: Combined preliminary–detailed design of wind turbines, Wind Energy Science, 1, 71–88, https://doi.org/10.5194/wes-1-71-2016, http://www.wind-energ-sci.net/1/71/2016/, 2016.

Bottasso, C. L. and Cacciola, S.: Model-independent periodic stability analysis of wind turbines, Wind Energy, 18, 865–887, https://doi.org/10.1002/we, http://onlinelibrary.wiley.com/doi/10.1002/we.1608/full, 2015.

Bottasso, C. L., Campagnolo, F., and Croce, A.: Multi-disciplinary constrained optimization of wind turbines, Multibody System Dynamics, 27, 21–53, https://doi.org/10.1007/s11044-011-9271-x, 2012.

Bottasso, C. L., Croce, A., Riboldi, C. E., and Nam, Y.: Multi-layer control architecture for the reduction of deterministic and non-deterministic loads on wind turbines, Renewable Energy, 51, 159–169, https://doi.org/10.1016/j.renene.2012.08.079, http://dx.doi.org/10.1016/j.renene.2012.08.079, 2013.

Dimitrov, N., Natarajan, A., and Mann, J.: Effects of normal and extreme turbulence spectral parameters on wind turbine loads, Renewable Energy, 101, 1180–1193, https://doi.org/10.1016/j.renene.2016.10.001, http://dx.doi.org/10.1016/j.renene.2016.10.001, 2017.

Døssing, M.: Optimization of Wind Turbine Rotors - Using Advanced Aerodynamic and Aeroelastic Models and Numerical Optimization, Ph.D. thesis, 2011.

Drela, M.: Viscous-Inviscid Analysis of Transonic and Low Reynolds Number Airfoils, AIAA Journal, 25, 1347–1355, 1987.

Drela, M.: XFOIL: An Analysis and Design System for Low Reynolds Number Airfoils, in: Low Reynolds Number Aerodynamics, edited by Mueller, T. J., pp. 1–12, Springer Berlin Heidelberg, Berlin, Heidelberg, 1989.

Dykes, K., Graf, P., Scott, G., Ning, A., King, R., Parsons, T., Damiani, R., Felker, F., and Veers, P.: An Integrated System Model of Wind Turbines and Plants Outline, http://www.nrel.gov/wind/systems{_}engineering/se{_}workshop{_}2015.html, 2015.

Griffith, D.: The SNL100-01 Blade: Carbon Design Studies for the Sandia 100-meter Blade, Tech. Rep. February, http://prod.sandia.gov/techlib/access-control.cgi/2013/131178.pdf, 2013a.

Griffith, D. T.: The SNL100-02 Blade : Advanced Core Material Design Studies for the Sandia 100- meter Blade, Tech. Rep. November, 2013b.

Griffith, D. T.: Update on SUMR-13 Rotor Cost Savings, Tech. rep., University of Texas Dallas, http://www.makeavailableifpossible.com, 2017.

Griffith, D. T. and Ashwill, T. D.: The Sandia 100-meter All-glass Baseline Wind Turbine Blade : SNL100-00, Tech. Rep. June, https://doi.org/Report No. SAND2011-3779, 2011.

Griffith, D. T. and Chetan, M.: Assessment of flutter prediction and trends in the design of large-scale wind turbine rotor blades, in: The Science of making Torque from Wind (Torque2018), 2018.

Griffith, D. T. and Richards, P. W.: The SNL100-03 Blade : Design Studies with Flatback Airfoils for the Sandia 100-meter Blade, Tech. Rep. September, Sandia Report, 2014.

Hayman, G. J.: MLife Theory Manual for Version 1. 00, Tech. rep., NREL, 2012.

Ichter, B., Steele, A., Loth, E., Moriarty, P., and Selig, M.: A morphing downwind-aligned rotor concept based on a 13-MW wind turbine, Wind Energy, 19, 625–637, https://doi.org/10.1002/we.1855, http://onlinelibrary.wiley.com/doi/10.1002/we.1608/fullhttp://www.ncbi.nlm.nih.gov/pubmed/21790082http://doi.wiley.com/10.1002/we.1855http://arxiv.org/abs/1006.4405, 2016.

International Electrotechnical Commission: IEC 61400-1: Wind Turbines - Part 1: Design Requirements, Tech. rep., 2005.

Jonkman, B. and Kilcher, L.: TurbSim User's Guide: Version 1.06.00, Tech. Rep. September, NREL, 2012.

Jonkman, J.: The New Modularization Framework for the FAST Wind Turbine CAE Tool, 51st AIAA Aerospace Sciences Meeting, Grapvine Texas, 2013.

Jonkman, J., Butterfield, S., Musial, W., and Scott, G.: Definition of a 5-MW reference wind turbine for offshore system development, Tech. rep., https://doi.org/10.1002/ajmg.10175, http://tethys-development.pnnl.gov/sites/default/files/publications/Jonkman{_}et{_}al{_}2009.pdf, 2009.

Jonkman, J. M. and Matha, D.: Dynamics of offshore floating wind turbines - analysis of three concepts, Wind Energy, 14, 557–569, https://doi.org/10.1002/we, http://onlinelibrary.wiley.com/doi/10.1002/we.1608/full, 2011.

Larwood, S. M. and Chow, R.: Comparison of upwind and downwind operation of the NREL Phase VI Experiment, Journal of Physics: Conference Series, 753, https://doi.org/10.1088/1742-6596/753/2/022041, 2016.

Loth, E., Steele, A., Qin, C., Ichter, B., Selig, M. S., and Moriarty, P.: Downwind pre-aligned rotors for extreme-scale wind turbines, Wind Energy, 20, 1241–1259, https://doi.org/10.1002/we.2092, 2017.

McFarlane, D. and Glover, K.: A loop-shaping design procedure using H/sub infinity / synthesis, IEEE Transactions on Automatic Control, 37, 759–769, https://doi.org/10.1109/9.256330, 1992.

McWilliam, M., Barlas, T. K., Madsen, H. A., and Zahle, F.: Aero-elastic Wind Turbine Design with Active Flaps for AEP Maximization, Wind Energy Sci., pp. 1–17, 2018.

Mone, C., Hand, M., Bolinger, M., Rand, J., Heimiller, D., and Ho, J.: 2015 Cost of Wind Energy Review NREL/TP-6A20-66861, Nrel, https://doi.org/NREL/TP-5000-52920, 2015.

Natarajan, A., Hansen, M. H., and Wang, S.: Design Load Basis for Offshore Wind turbines: DTU Wind Energy Report No. E-0133, Tech. rep., 2016.

Ning, A., Damiani, R., and Moriarty, P. J.: Objectives and Constraints for Wind Turbine Optimization, Journal of Solar Energy Engineering, 136, 041 010, https://doi.org/10.1115/1.4027693, http://solarenergyengineering.asmedigitalcollection.asme.org/article.aspx?doi=10.1115/1.4027693, 2014.

Noyes, C., Qin, C., and Loth, E.: Measurements of Wind Turbine Tower Shadow and Fairing Effects, in: 2018 Wind Energy Symposium, January, https://doi.org/10.2514/6.2018-1244, https://arc.aiaa.org/doi/10.2514/6.2018-1244, 2018.

Paquette, J.: Structural Design of the SUMR-13 Wind Turbine Blade, Tech. rep., Sandia National Laboratories, http://www.makeavailableifpossible.com, 2017.

Pavese, C., Tibaldi, C., Larsen, T. J., Kim, T., and Thomsen, K.: Reduced Design Load Basis for Ultimate Blade Loads Estimation in Multidisciplinary Design Optimization Frameworks, Journal of Physics: Conference Series, 753, https://doi.org/10.1088/1742-6596/753/6/062005, 2016.

Pavese, C., Tibaldi, C., Zahle, F., and Kim, T.: Aeroelastic multidisciplinary design optimization of a swept wind turbine blade, Wind Energy, 20, 1941–1953, https://doi.org/10.1002/we.2131, 2017.

Peeringa, J., Brood, R., Ceyhan, O., Engels, W., de Winkel, G., and Winkel, G. D.: Upwind 20MW Wind Turbine Pre-Design: Blade design and control, ECN-E–11-017 December, pp. 1–53, 2011.

Robertson, A., Sethuraman, L., Jonkman, J., and Quick, J.: Assessment of Wind Parameter Sensitivity on Ultimate and Fatigue Wind Turbine Loads Preprint, 2018.

Schorbach, V., Dalhoff, P., and Gust, P.: Teeter design for lowest extreme loads during end impacts, Wind Energy, pp. 1–14, https://doi.org/10.1002/we.2140, http://doi.wiley.com/10.1002/we.2140, 2017.

Selig, M.: PROPID – Software for Horizontal-Axis Wind Turbine Design and Analysis, http://www.ae.illinois.edu/m-selig/propid.html, 1995-.

Selig, M. and Tangler, J.: Development and application of a multipoint inverse design method for horizontal axis wind turbines, Wind Engineering, 19, 91–105, 1995.

Sieros, G., Chaviaropooulos, P., Sørensen, J. D., Bulder, B. H., and Jamieson, P.: Upscaling wind turbines: theoretical and practical aspects and their impact on the cost of energy, Wind Energy, 15, 3–17, https://doi.org/10.1002/we, http://onlinelibrary.wiley.com/doi/10.1002/we.1608/full, 2012.

Tibaldi, C., Hansen, M. H., and Zahle, F.: Methods for systematic tuning of wind turbine controllers, Tech. rep., 2015.

van der Tempel, J. and Molenaar, D. P.: Wind turbine structural dynamics-a review of the principles for modern power generation, onshore and offshore, Wind Engineering, 26, 211–222, 2003.

van Solingen, E. and van Wingerden, J. W.: Linear individual pitch control design for two-bladed wind turbines, Wind Energy, 18, 677–697, 2015.

van Solingen, E., Beerens, J., Mulders, S. P., De Breuker, R., and van Wingerden, J. W.: Control design for a two-bladed downwind teeterless damped free-yaw wind turbine, Mechatronics, 36, 77–96, https://doi.org/10.1016/j.mechatronics.2016.03.008, 2016.

Zahle, F., Tibaldi, C., Verelst, D. R., Bak, C., Bitche, R., and Albegaria Amaral Blasques, J. P.: Aero-Elastic Optimization of a 10 MW Wind Turbine, AIAA SciTech, 33rd WInd Energy Symposium, p. 23, https://doi.org/10.2514/6.2015-0491, 2015.

Zalkind, D. S., Pao, L. Y., Martin, D. P., and Johnson, K. E.: Models used for the simulation and control of a segmented ultralight morphing rotor, in: Preprints of the 20th World Congress, pp. 4564–4569, Toulouse, France, https://doi.org/10.1016/j.ifacol.2017.08.377, 2017.